GZMK^{high} CD8^{+} T effector memory cells are associated with CD15^{high} neutrophil abundance in early-stage colorectal tumors and predict poor clinical outcome.

Silvia Tiberti[1], Carlotta Catozzi[1], Caterina Scirgolea[2], Ottavio Croci[3], Mattia Ballerini[1], Danilo Cagnina[1], Chiara Soriani[1], Carina B. Nava Lauson[1], Angeli D. Macandog[1], Giovanni Bertalot[4], Wanda L. Petz[5], Simona P. Ravenda[6], Valerio Licursi[7], Paola Paci[7], Marco Rasponi[8], Nicola Fazio[6], Guangwen Ren[9], Uberto Fumagalli-Romario[5], Martin H. Shaefer[1], Stefano Campaner[3], Enrico Lugli[2,10], Luigi Nezi[1*] and Teresa Manzo[1*#].

[1] Department of Experimental Oncology, European Institute of Oncology- IRCCS, Milano, Italy

[2] Laboratory of Translational Immunology, Humanitas Clinical and Research Center-IRCCS, Milan, Italy

[3] Center for Genomic Science of IIT, CGS@SEMM (Istituto Italiano di Tecnologia at European School of Molecular Medicine), Fondazione Istituto Italiano di Tecnologia (IIT), Milan, Italy.

[4] APSS Trento Hospital & Health Care, Trento, Italy

[5] Gastrointestinal Surgery Division, European Institute of Oncology-IRCCS

[6] Division of Gastrointestinal Medical Oncology and Neuroendocrine Tumors, European Institute of Oncology-IRCCS

[7] Department of Computer, Control and Management Engineering, Sapienza - University of Rome

[8] Department of Electronics, Information and Bioengineering, Politecnico di Milano, Milan, Italy

[9] The Jackson Laboratory Cancer Center, Bar Harbor, ME, USA.

[10] Humanitas Flow Cytometry Core, Humanitas Clinical and Research Center – IRCCS, Milan, Italy.

[*] LN and TM contributed equally.

[#] Leading contact: teresa.manzo@ieo.it

ABSTRACT

Tumor contexture has emerged as a major determinant to establish prognosis and guide novel therapies and tumor infiltrating $CD8^+$ T cells have been associated with a better prognosis in several solid tumors, including early-stage colorectal cancer (CRC). However, the tumor immune infiltrate is highly heterogeneous and understanding how the interplay between different immune cell compartments impacts on the clinical outcome is still in its infancy.

Here, we describe in a prospective cohort a novel $CD8^+$ T effector memory population, which is characterized by high levels of Granzyme K ($GZMK^{high}$ $CD8^+$ T_{EM}) and correlated with $CD15^{high}$ tumor infiltrating neutrophils. We provide both *in vitro* and *in vivo* evidence of the role of stromal cell-derived factor 1 (CXCL12/SDF-1) in driving functional changes on neutrophils at the tumor site, promoting their retention and increasing crosstalk with $CD8^+$ T cells. Mechanistically, as a consequence of the interaction with neutrophils, $CD8^+$ T cells are skewed towards a $CD8^+$ T_{EM} phenotype, producing high levels of GZMK, which in turn decreased E-cadherin pathway. The correlation of $GZMK^{high}$ $CD8^+$ T_{EM} and neutrophils with both tumor progression in mice and early relapse in CRC patients demonstrate the role of $GZMK^{high}$ $CD8^+$ T_{EM} in promoting malignancy. Indeed, a gene signature defining $GZMK^{high}$ $CD8^+$ T_{EM} was associated with worse prognosis on a larger independent cohort of CRC patients and a similar analysis was extended to lung cancer (TCGA).

Overall, our results highlight the emergence of $GZMK^{high}$ $CD8^+$ T_{EM} in early-stage CRC tumors as a hallmark driven by the interaction with neutrophils, which could implement current patient stratification and be targeted by novel therapeutics.

KEYWORDS

$CD8^+$ T effector memory cells

Granzyme K

Neutrophils

Colorectal cancer

Tumor microenvironment

66 **BACKGROUND**

67 Colorectal cancer (CRC) is the third most commonly diagnosed tumor worldwide and a
68 leading cause of death for cancer, with the efficacy of treatment and subsequent survival
69 largely dictated by the tumor-node-metastasis (TNM) stage at diagnosis. Tumor contexture
70 has emerged as a major determinant to establish prognosis and guide novel therapies
71 (Galon et al., 2014; Pagès et al., 2009a). However, despite favorable TNM staging and
72 significant lymphocyte infiltration (Ogino et al., 2009), 30-40% of patients treated for early-
73 stage CRC relapse and ultimately die from metastatic disease (American Cancer Society,
74 2018), demonstrating the inadequacy of current stratification.

75 In this regard, tumor infiltration by cytotoxic $CD8^+$ T cells has been associated with a better
76 prognosis in several solid tumors, including CRC (Fountzilas et al., 2018; Koch et al., 2006)
77 and high levels of memory $CD8^+$ T cells prevent early metastatic invasion and are associated
78 with better survival (Pagès et al., 2009b), supporting the idea that the intratumor immune
79 landscape contributes to tumor control and prevention of recurrence. However, the tumor
80 immune infiltrate is highly heterogeneous and, although the influence of various myeloid cell
81 populations on T cell activity has been reported (Binnewies et al., 2018; Lavin et al., 2017;
82 Salmon et al., 2016), our understanding of the interplay between different cell compartments
83 at the tumor site and their impact on the clinical outcome is still in its infancy. In particular,
84 tumor-associated neutrophils represent a significant fraction of the inflammatory cells in the
85 tumor microenvironment (TME) of many types of cancers, including CRC (Berry et al., 2017;
86 Carus et al., 2013; Ilie et al., 2014; Li et al., 2018; Rao et al., 2012; Silvestre-Roig et al.,
87 2019). The concept of neutrophil phenotypic and functional diversity has emerged from
88 murine tumor models (Ballesteros et al., 2020), but the existence of subsets of infiltrating
89 neutrophils with different functions in humans is still debated. As a result, the contribution of
90 these cells to inhibiting or promoting tumor progression by reshaping anti-tumor immune

response remains largely unexplored and often contradictory in humans (Gentles et al., 2015; Singhal et al., 2016).

Here, we sought to gain insight into the crosstalk between the TME and immune cells to elucidate their contribution to relapse and implement patient's stratification for subsequent immune-based therapeutics. We have estimated heterogeneity of immune cells within and across CRC patients by employing multiparametric flow cytometry and single-cell transcriptomics, obtaining functional information. This combined approach has revealed an association of neutrophils infiltrating the tumor with a unique immune signature of tumor infiltrating lymphocytes (TILs), which is characterized by high levels of Granzyme K (GZMK) expression and leads to worse prognosis.

METHODS

Study approval.

Tumors, adjacent normal tissue and peripheral blood samples from patients diagnosed with CRC at European Institute of Oncology (IEO), were collected with written informed consent as approved by the Internal Research Center Review Board. All patients were treatment-naïve at the time of sample collection (Table 1) and fresh tissue was collected the day of the surgery. All donors provided their consent in accordance with the Declaration of Helsinki.

Mice were obtained from Charles River, housed and bred in a specific pathogen free animal facility. The experiments described in this manuscript were performed in accordance with the European Union Guideline on Animal Experiments. Mouse protocols were approved by the Italian Ministry of Health, the IEO Committee and the Institutional Animal Care and Use Committee of The Jackson Laboratory. Mice were matched for age and sex in each experiment.

117 **Tissue dissociation and cells.**

118 Primary tumors (T) and Normal Adjacent Tissue (NAT, collected at 10cm from the tumor
119 site) were dissociated into single-cell suspension by mechanical and enzymatic
120 disaggregation. The samples were then filtered through 70-µm cell strainers and washed in
121 PBS without Ca^{2+} and Mg^{2+}. Interstitial fluid was prepared from T and NAT. Briefly, tissues
122 were minced in cold PBS and incubated on ice until cellular debris was precipitated. The
123 supernatant was collected and spinned at 1200g at 4ºC and then used fresh or stored at -
124 80ºC.

125 Peripheral blood mononuclear cells (PBMCs) were isolated via density-gradient separation
126 with Ficoll. Total $CD8^+$ T cells were enriched by negative magnetic separation using the
127 Miltenyi $CD8^+$ T Cell Isolation Kit Human. Human polymorphonuclear leukocytes (PMNs)
128 enriched pellets were diluted with PBS and 3% dextran solution in HBSS was added in a
129 1:1 ratio. After centrifugation, the supernatant was processed for red blood cell lysis
130 according to manufacturer's instructions (Red Blood Cell Lysis Solution, Miltenyi). Cells
131 were either used fresh or cryopreserved according to standard procedures. Mouse
132 neutrophils and $CD8^+$ T cells were purified according to manufacturer's instructions using
133 anti-Ly6G and $CD8^+$ T Cell Isolation Kit Mouse, respectively (Miltenyi Biotech). Purity of
134 isolated human and mouse immune populations were checked by FACS (>95%).

135

136 ***In vitro* CD8⁺ T Cells and Neutrophils co-culture.**

137 $CD8^+$ T cells activated with plate-bound anti-human CD3 (2mg/mL) and anti-human CD28
138 (2mg/mL) and freshly isolated neutrophils were co-cultured at different ratios in complete
139 RPMI-1640 media.

140

141 ***In vitro* GZMK and SDF1 treatments.**

142 HT-29 and CACO2 cells were cultured in transwells in a ratio 1:9 (CACO2:HT-29) for 16
143 days when trans-epithelial electrical resistance (TEER) was measured to assess the
144 epithelial formation. Cells were treated with rHu-GZMK 10uM for 24h. For treatment of
145 neutrophils, freshly isolated cells were treated with rHu-GZMK 10uM or SDF1 100ng/ml and
146 analyzed at different time points as indicated in the relative figure legend.
147
148 **Neutrophils migration assay.**
149 Neutrophil migration assays were performed using a custom-made microfluidic device in
150 PDMS composed by three parallel channels (height 200µm, length 1.1cm, width central
151 channel 1300µm, lateral channels 700µm) separated by two lines of trapezoidal pillars. The
152 central channel was used to confine a collagen matrix gel, the right channel for cell injection
153 and the left channel for treatments. PBS 10X, HEPES 80mM, NaOH 1N, 8.04mg/ml rat tail
154 Collagen type I (Corning) and RPMI culture medium (without phenol red) were mixed on ice
155 to obtain a collagen matrix solution. The collagen solution was injected in the central channel
156 of the microfluidic chip and incubated at 37°C to allow the complete reticulation of the
157 collagen matrix. The collagen matrix was hydrated by injecting culture medium into the
158 lateral channels of the device. Culture medium was added to the reservoirs to avoid
159 evaporation and chips were incubated at 37°C. Purified human neutrophils ($3x10^6$/ml) from
160 healthy donor were labeled with calcein-AM (green), Hoechst 33342 (blue), and DRAQ7
161 (red) and injected in the right channel of the microfluidic devices. The microfluidic chips were
162 incubated at 37°C for 20 minutes on an angled surface (30 degrees) to allow neutrophils to
163 lie at the interface between the lateral channel and the collagen gel. Chemoattractant
164 solutions or culture medium were added to the left channel and time lapse experiments were
165 performed using Nikon Eclipse Ti (3 fields for chip, 1 image every 2.30min for 4h at 10X
166 magnification) to evaluate invasion of neutrophils in the collagen gel. Interstitial fluid from T
167 and NAT of LN and HN patients, purified CXCL6 (400ng/ml), SDF-1 (100ng/ml) and IL-8

168 (100ng/ml) were tested. Migrating cells were counted and analyzed using ImageJ version
169 2.0.
170
171 **Neutrophils Gelatinase assay.**
172 The gelatinase activity was measured from control or SDF1 (100 ng/mL) treated
173 neutrophils in triplicate, using DQ gelatin (molecular Probes, 100 µg/mL final
174 concentration) following manufacturer's recommendations. The fluorescent output was
175 measured every 15 min at room temperature on a GloMax Discover (Promega Instrument)
176 microplate reader (Ex= ~495 nm, Em= ~515 nm) and corrected for background.
177 *Clostridium histolyticum* collagenase (0.15 U/mL) was used to generate an internal
178 calibration curve.
179
180 **Neutrophils Adhesion assay.**
181 Purified human neutrophils were labeled with calcein-AM (green), Hoechst 33342 (blue) for
182 20 minutes at 37°C, as previously described (Htwe et al., 2018). After washing, neutrophils
183 were incubated in RPMI media with or without SDF1 (100 ng/mL) for 1 hour at 37°C in a 96-
184 well on a monolayer of human micro-endothelial cells (HMEC1). After two gentle washes
185 with PBS to remove non-adherent cells, images of three fields were recorded for each well
186 using an EVOS microscope (EVOS FL Cell Imaging System) at 4x magnification. Adherent
187 neutrophils were measured by counting calcein positive neutrophils using ImageJ version
188 2.0.0.
189
190 **Multiparametric flow cytometry and sorting.**
191 High-dimensional flow cytometry was performed on T, NAT and PB. Conjugated antibodies
192 used for flow cytometry are shown in Table 2. Briefly, single-cell suspensions were stained
193 fresh or after thawing in pre-warmed RPMI with 10% FBS. Cells were washed in staining

194 buffer (PBS with 2%FBS and 2mM EDTA) and incubated for 30min at 4°C with surface
195 antibody cocktail in staining buffer, washed twice in staining buffer, fixed and permeabilized
196 using Fixation/Permeabilization Solution Kit (BD, Cat # 554714), and stained intracellularly
197 for 1h at 4°C with an antibody cocktail in the permeabilization solution. Samples were
198 acquired using a FACSymphony A5 or a FACSCelesta BVYG equipped with FACSDiva
199 software version 8.0.1 (all from BD Biosciences). Compensation Beads (ThermoFisher,
200 Cat# 01-2222-41) were used to prepare single-stained controls for electronic compensation.
201 Dead cells were excluded using Fixable Viability Stain (BD). To evaluate ex vivo cytokines
202 production, CD8+ T cells were stimulated 3 h with PMA (20ng/mL), ionomycin (1ug/mL) and
203 GolgiPlug protein-transport inhibitor (brefeldin A, 1:1000). CD8 T cell subsets were sorted
204 to high purity using FACSAria III (BD Biosciences).
205 All the FCS files generated were analyzed and visualized with software FlowJo v10
206 (TreeStar). RPhenograph (Levine et al., 2015) package was used to analyze the
207 multiparametric data from CRC patients derived T, NAT and PB. CD8 analysis was
208 performed on 3000 events per sample after manual gating isolation of singlet, LD negative,
209 CD45+CD3+CD8+ T cells. All samples were concatenated by the "cytof_exprsMerge
210 function". The number of nearest neighbors identified in the first iteration of the algorithm, K
211 value, was set to 100. UMAP and tSNE representation were generated and visualized using
212 FlowJo version 10 (FlowJo). Under-represented clusters (<0.5%) were discarded in
213 subsequent analysis. The balloon plots, performed using the ggplots2 R package, generat
214 a further metaclustering classification, interpolating MFI and frequency of each marker per
215 cluster. MFI were multiplied to derive the integrated MFI (iMFI, rescaled to values from 0 to
216 100). Euclidean distance and Ward-linkage methods via cytofkit package were applied to
217 generate hierarchical metaclustering of Phenograph generated clusters.
218
219 **Bead-based multiplexed ELISA.**

220 Multiplexed ELISA on interstitial fluid from matched T and NAT fresh tissues were performed
221 on a Luminex 200 platform (Luminex Inc.,) using custom kits of pre-mixed antibody-coated
222 beads (R&D System Inc., MN), which included the following analytes: CCL11_eotaxin,
223 CCL13_MCP4, CCL17_TARC, CCL2_MCP1, CCL22_MDC, CCL26_EOTAXIN3,,
224 CCL5_RANTES, CCL8_MCP2, CD25_IL2Ra, CX3CL1_FRACTALKINE, CXCL1_GROa,
225 CXCL10_IP10, CXCL11_ITAC1, CXCL13_BLC_BCA1, CXCL4_PF4, CXCL5_ENA78,
226 CXCL6_GCP2, EGF, IFNg, GMCSF, HGF, IL10, IL1ra_IL1F3, IL7, IL8_CXCL8, TRAIL,
227 VEGFA, IL1b_IL1F2, IL5, IL6, IL-17F, IL22, IL23, TNFa, LXSAHM-01, CCL3_MIP1a,
228 CCL4_MIP1b, FGFbasic_FGF2, GCSF, IL1a_IL1F1, IL2, IL4, IL-12 p70, IL13, IL15, IL-
229 17/IL17A, CXCL12_SDF1 , TGFB1, TGFB3. The assay was runned based on manufacturer
230 reccomendations. Briefly, 50ul of samples together with kit standards were added to each
231 well in duplicate and incubated with the diluted Microparticle Cocktail at 4C, ON, on a shaker
232 at 850rpm. Unbound soluble molecules were removed by washing the plate. The Biotin-
233 Antibody Cocktail specific to the analytes of interest was added to each well for 1h at RT.
234 After washing again, the Streptavidin-Phycoeriythrin conjugated was added for 30 minutes
235 at RT. After the final washing steps, the microparticles are resuspended in kit buffer and
236 read on a Luminex 200 platform. The outputs (pg/mL) were visualized and statistically
237 analyzed in R upon centering and scaling using the scale function in R (SD from mean
238 pg/mL). Data were visualized together with sample annotations using the ComplexHeatmap
239 package. Group comparisons were visualized as boxplots using the ggpubr package and
240 statistically analyzed by applying the non-parametric Wilcoxon signed-rank test on the
241 values, where significance is set at p-value < 0.05. Soluble molecule data were associated
242 with other experimental data by Spearman correlation and visualized using the corrplot
243 package.
244
245 **Immunohistochemistry (IHC) and Immunofluorescence (IF).**

246 Slides (5um) from formalin-fixed paraffin embedded (FFPE) samples were processed for
247 deparaffinization and rehydration. Heat-induced antigen retrieval (citrate buffer pH 6 or 9 –
248 Thermofisher) was performed using the microwave. 3% H_2O_2 incubation was used for IHC
249 preparation. Slides were incubated ON at 4°C with mouse anti-human CD66b antibody
250 (BioLegend, 305102, 1:100 for both IHC and IF), anti-human CD8 (Invitrogen, 53-0008-82,
251 1:100), rabbit anti-human GRZMK (Invitrogen, LS-C119554-50, 1:100), rabbit anti-human
252 E-cadherin (Abcam, Ab1416, 1:100), rat anti-human Ki67 (Ebioscience, SolA15, 1:200),
253 rabbit anti-human EPCAM (Abcam, Ab32394, 1:400), mouse anti-human SDF1 (R&D,
254 MAB350, 1:100), anti-human αSMA (Abcam, Ab8211, 1:200) in a blocking solution
255 composed of 3% BSA, 5% goat serum (Invitrogen, 10000C) and 0,1% Triton in PBS. After
256 incubation with HRP-secondary antibody (30min) and Aminoethyl Carbazole (AEC) + High
257 Sensitivity Substrate Chromogen (Dako) (for IHC) or fluorophore conjugated antibodies
258 (Invitrogen, A32723, goat anti-mouse 488; Invitrogen, A21247, goat anti-rabbit 647;
259 Invitrogen, A21206, goat anti-rabbit 488; Invitrogen, A21424, goat anti-mouse 555; 1:500;
260 Invitrogen, A21434, goat anti-rat 555, all 1:500 for 1 hour at RT), slides were mounted and
261 acquired by using Aperio or SP8 confocal microscope (Leica), respectively.
262
263 **Imaging analysis.**
264 For quantification of GZMK signal on human colorectal cancers, sections were labeled with
265 DAPI, anti-GZMK, anti-CD66b and Alexa Fluor 488-conjugated anti-CD8 primary antibodies
266 and images captured with a Nikon CSU-W1 spinning disk (Nikon Europe BV) using a
267 40X/1.15 NA water immersion objective lens (pixel size 0.1625 x 0.1625 um^2). For the tumor
268 area identification, previews of tissue sections on the DAPI channel were acquired with a
269 10X/0.3 NA dry objective lens. Inside the tumor areas, 3 to 4 regions were randomly chosen
270 for the acquisition with a 40X/1.15 NA water immersion objective lens. Each region was
271 made of 12 adjacent tiles covering a total area > 4 mm^2 per tissue section.

272 The quantification of the GZMK signal in $CD8^+$ cells was done with a custom-made Fiji macro
273 (Schindelin et al., 2012). Briefly, images were pre-processed with denoising and background
274 subtraction, and nuclei were segmented on the DAPI channel with the plugin StarDist
275 (Schmidt et al., 2018), using the built-in model Versatile (fluorescent nuclei) and the intensity
276 parameters, including “mean intensity” and “raw integrated density”, of CD8, GZMK and
277 CD66b fluorescence were quantified in a band of thickness 1 um around each nucleus.
278 Statistical analysis was performed in R. $CD8^+$ cells were identified from the database by
279 setting criteria on the intensity parameters of the specific fluorescence. Particularly, a cell
280 was considered as positive for CD8 fluorescence channel if its “raw integrated density” was
281 above a threshold value, set by the comparison in images of the “raw integrated density”
282 values of cells expressing CD8 fluorescence and the “raw integrated density” of cells
283 expressing only autofluorescence signal. Moreover, a further correction regarding the cells
284 that had the band around the nucleus overlapping with red blood cells was applied: the ratio
285 of the “raw integrated density” in the green channel versus the red channel was computed
286 and only cells with a ratio green/red > 4 were considered as positive for CD8. The same
287 procedure described above was used for the detection of CD66b positive cells (for red blood
288 cells correction a ratio red/green > 2 was set to consider cells as CD66b positive).
289 Differences between two groups were calculated by unpaired, two-tailed Student's t test.
290 The analysis of GZMK fluorescence in CD8+ cells lying in the proximity of a neutrophil
291 ($CD66b^+$) was performed as follows: the distance between a $CD8^+$ cell and its nearest
292 neutrophil was computed per each field of view. Only distances below 10 um were taken
293 into account to select pairs of CD8+ cell-neutrophil that were close to each other. The mean
294 intensity of GZMK fluorescence in CD8+ cells close to neutrophils was compared to the
295 GZMK mean intensity of cells close to neutrophils that were not positive for CD8.
296 For the quantification of SDF-1 in cells positive for αSMA, human colorectal cancers sections
297 labeled with DAPI, anti-SDF-1, anti-αSMA and anti-EPCAM primary antibodies, and

298 captured with a Nikon Eclipse Ti widefield microscope (Nikon Europe BV) using a 20X/0.75
299 NA dry objective lens (pixel size 0.32 x 0.32 um^2). For the tumor area's identification,
300 previews of tissue sections were acquired with a 4X/0.2 NA dry objective lens. Inside the
301 tumor areas, regions were randomly chosen for the acquisition with 20X/0.75 NA dry
302 objective lens for a total acquired area > 35 mm^2 per tissue section.
303 The quantification of SDF-1 signal in αSMA^+ cells was done with Qupath v. 0.2.3 (Bankhead
304 et al., 2017) through a custom-made script. Briefly, cell nuclei were detected on DAPI
305 channel with the StarDist extension and a cell expansion of 1 um was applied in order to
306 measure fluorescence in the cytoplasmic/membrane cell's area. For the nuclei segmentation
307 with StarDist, a custom model was trained and tested using the StarDist (2D) network in
308 ZeroCostDL4Mic (von Chamier et al., 2021): a training dataset was generated by the manual
309 annotation of nuclei in QuPath and labeled images were exported for the deep-learning
310 training; the model's training and quality control assessment were performed with the
311 StarDist (2D) notebook. For the detection of pixels positive for αSMA staining, a pixel
312 classifier was created with the QuPath's function Create thresholder and the quantification
313 of the positive area inside each segmented cell was added as a measurement parameter in
314 the detection's results table. Other two-pixel classifiers in the red and far-red channels were
315 similarly created to be used in the statistical analysis step. The expression of SDF1 was
316 quantified as the mean intensity of the corresponding fluorescence signal in the band around
317 the nucleus.
318 Statistical analysis was performed in R. Cells with an area > 3 um2 (estimated as the 10%
319 of the area of a band created around a nucleus with area size 46 um2) of pixels classified
320 as positive for αSMA were considered as αSMA+. Cells overlapping with red blood cells
321 were discarded from the analysis when presenting positive area > 0 um2 for the pixel
322 classifiers in green, red and far-red channels. Differences between two groups were
323 calculated by unpaired, two-tailed Student's t test.

324

325 **scRNA-seq.**

326 T and NAT single cell suspension after counting was resuspended in PBS without Ca2+ and
327 Mg2+ with 0.04% BSA. Approximately 2,000 cells/ul from each sample were used for the
328 analysis. Briefly, every sample was loaded into one channel of Single Cell Chip A using a
329 Chromium Single Cell 3′ v2 Reagent Kit (10x Genomics). After capture and lysis,
330 complementary DNA was synthesized and amplified over 14 cycles according to the
331 manufacturer's protocol (10x Genomics). Libraries were prepared from 50 ng amplified
332 cDNA. Sequencing was performed using a NovaSeq 6000 System (Illumina). An average
333 sequencing depth of at least 50,000 reads per cell was obtained for each sample.

334

335 **scRNAseq analysis.**

336 Single cells of samples from 11 patients (each one sequenced in the far tumor (D) and tumor
337 site (T)) were sequenced with the 3' v3 chemistry and aligned using Cellranger count v. 3.1
338 on human genome hg38. Only droplets with a minimum number of unique molecular
339 identifiers (UMI) were considered as "cells"; this was done by default by the Cellranger
340 program.

341 We carried out a preliminary analysis using data of all the samples collected from the 11
342 patients (D and T, total of 89715 cells, data not shown). Based on total cells in each patient
343 and the distribution of each patient's cells within groups identified by UMAP, we excluded
344 patients 3, 8 and 6 from further analyses. Thus, 52316 cells were processed.

345 We used the Seurat v. 3 R package to analyse single cell data (Stuart et al., 2019). To
346 identify cell populations or sub-populations, uniform manifold approximation and projection
347 (UMAP) was carried out from the first principal components of the PCA based on the
348 expression of the most variable genes, normalized using SCT transformation as suggested
349 in Seurat documentation ("SCTransform" function, (Hafemeister and Satija, 2019). The

350 different clusters in UMAPs were found using nearest neighbor clustering (SNN) with the
351 function “FindClusters” of the Seurat package. In particular:
352 a) For global cell population (52316 cells, fig. Supp. 6A): for UMAP, the first 30 principal
353 components were used, and n.neighbors=60, min.dist=0.005 were set. For SNN clustering,
354 top 20 principal components were used, with other parameters k.param=10,
355 prune.SNN=1/10. The resolution used in the “FindClusters” function was set to 0.11.
356 b) For T/NK cells (8716 cells, fig. Supp. 6E): cells belonging to the “T/NK" cluster of the
357 previous step (a) were used. The UMAP was built using the first 30 principal components
358 and n.neighbors=40, min.dist=0.002 were set as parameters. SNN clustering was carried
359 out as above (a) but with a resolution of 0.09 in the “FindClusters" function. Finally, cells
360 with the first UMAP dimension (UMAP_1) > 8 were considered as outliers and removed.
361 c) To further characterize T CD8+ cell subtypes (fig. 6A), cells belonging to the clusters 3
362 and 4 were extracted from the previous step (b) and the UMAP was built using the first 15
363 principal components from the expression of the following cell-specific markers that
364 presumably would identify the expected subtypes:
365 TRDC, PRF1, CD3D, CD3E, TRGC1, TRGC2, LEF1, IL6R, NOSIP, SELL, CCR7, CD4,
366 BATF, TIGIT, FOXP3, TNFRSF4, CD8A, CD8B, GZMH, FGFBP2, GZMB, GNLY, ZEB2,
367 HLA-DRB5, CX3CR1, GZMA, IFNG, CCL4, SBF2, KLRB1, LTB, IL7R, FOS, CD40LG,
368 DPP4, IRF1, GZMM, GZMK, HLA-DRB1, HLA-DRA, CCL5, CTLA4, PDCD1, HAVCR2,
369 LAG3, CD38, ENTPD1, LAYN, CXCL13, TOX. Other parameters for the UMAP were
370 n.neighbors=20, min.dist=0.01. For SNN clustering, the top 15 principal components were
371 used, with other parameters being k.param=10, prune.SNN=1/10. The resolution parameter
372 in the “FindClusters” function was set to 0.5.
373 Differential expression of genes between different cell subgroups was carried out with the
374 “FindMarkers” function in the Seurat package, using the Wilcoxon test. Thresholds were set
375 to log2FC=0.25 and adjusted p value=0.05. For Figures 6C, 6F and Supp. 7D and E the

376 size of the points corresponds to the score of the specific signature; this score is defined,
377 for each cell, as the sum of the counts of the genes belonging to a specific signature / the
378 total sum of the counts of that cell. The points with the biggest size correspond to a score
379 higher than 80% of the distribution of the scores of all the cells.
380 Cell types in the entire population (Fig. Supp 6A) were identified with the help of scMCA
381 (single cell mouse cell atlas) package (Sun et al., 2019) and then evaluating the expression
382 of the cell type specific markers. Pseudotime analysis (fig. 6E) was done using Monocle v.
383 3.
384
385 ***In vivo* animal experiments.**
386 C57BL/6J were subcutaneously injected with 1 × 10^6 MC38 cells/mouse. Animals were
387 euthanized when the tumor reached the volume of <1cm^3 and >1cm^3 to evaluate CD8$^+$ T
388 cell and neutrophil infiltration during progression. Blood was collected and spleen and
389 tumors harvested and dissociated to a single cell suspension. Tumors were digested (1,5
390 mg/mL collagenase, 0,75 mg/mL hyaluronidase and 0,1 mg/mL DNaseI) in RPMI 10% FBS
391 at 37°C. Cell suspension was filtered through 70-µm cell strainers, washed, counted and
392 stained for multiparametric flow cytometry.
393
394 **Survival analysis methods.**
395 We investigated the interplay between immune cytolytic activity and neutrophils infiltration
396 on overall (OS) and disease-free survival (DFS) in the colon adenocarcinoma cohort
397 (COAD) of The Cancer Genome Atlas (TCGA) (Weinstein et al., 2013) by performing a
398 Kaplan-Meier analysis. The cytolytic activity index was quantified by computing the
399 geometric mean of granzyme A and perforin expression (Rooney et al., 2015) and samples
400 were split according to the Maximally Selected Ranks Statistics cutoff ("maxstat", version
401 0.7-25). Neutrophils relative abundance was obtained by running CIBERSORTx (Rooney et

402 al., 2015) with a validated leukocyte gene signature matrix (LM22) on RNAseq data of COAD
403 samples. Samples were divided into two groups according to the presence or absence of
404 Neutrophils. Similarly, CIBERSORTx-derived gene expression signature was employed to
405 infer the GZMK^{high} cell subtype' abundance and analyze its association with survival. First,
406 the single-cell raw counts matrix of CD8^{+}Tem population was split into two subgroups
407 expressing "high" or "low" values of GZMK and used it to feed CIBERSORTx, building a
408 gene signature able to discriminate the two cell sub-populations. Secondly, we collected
409 survival tables of TCGA-COAD and TCGA-LUAD cohorts from cBioPortal (Cerami et al.,
410 2012) and ran Kaplan-Meier analysis stratifying patients with "high" and "low" infiltration of
411 CD8^{+} Tem cells expressing high levels of GZMK. Survival analyses were carried out on R
412 software version 4.0.5), by using "survival" (version 3-2-11) and "survminer" (version 0.4.9)
413 packages.
414
415 **Statistics and Data visualization.**
416 Results were analyzed and visualized on Prism version 9.2.0 (GraphPad). All statistical
417 analyses were conducted using GraphPad Prism version 9.2.0 or R software version 4.0.2.
418 Differences between two groups were calculated by two-tailed Student's t test. Multiple
419 comparisons were performed by one-way ANOVA followed by Bonferroni's multiple
420 comparison tests. Significance was set at P values ≤ 0.05. For all figures: *, P ≤ 0.05–0.01;
421 **, P ≤ 0.01–0.001; ***, P ≤ 0.001–0.0001; ****, P ≤ 0.0001. Unless noted in the figure legend,
422 all data are shown as mean ± SEM. The n numbers for each experiment and the numbers
423 of experiments are noted in the figure legends.
424
425
426 **RESULTS**

427 **Early-stage CRC patients can be stratified based on the abundance of CD15^{high}**
428 **neutrophils in the tumor microenvironment.**
429 Despite consistent T cell infiltration, over a third of early-stage CRC patient relapse,
430 suggesting that the anti-tumor immune response is somehow “leaky”. In this regard,
431 characterizing the heterogeneity of immune cells within and across CRC patients would be
432 essential to fully understand the mechanisms behind immune evasion. We profiled
433 peripheral blood (PB), tumor (T) and normal adjacent tissue (NAT >10 cm from tumor tissue)
434 from treatment-naïve patients (n= 42) with early-stage CRC (8th ed. AJCC stages I, II and
435 III) undergoing surgical resection (Figure 1A). Details of all patients involved in the study are
436 summarized in Table 1. Among the infiltrating innate immune cell populations, we observed
437 no significant difference on dendritic cells (DCs), lower proportion of NK cells in T compared
438 to NAT and enrichment in macrophages in T, albeit they were present at low frequencies
439 (Figure Supp. 1A). On the other hand, neutrophils were higher in T compared to NAT both
440 in number and frequency, as assessed by IHC (CD66b^{+}, Figure Supp. 1B) and FACS
441 (Figures 1B) (Bronte et al., 2016; Gustafson et al., 2015), respectively. Neutrophils were
442 identified as CD45^{+}CD11b^{+}CD15^{+} cells along with intermediate/low expression of CD33 and
443 negative staining for HLA-DR (Figure Supp. 1C) (Gustafson et al., 2015). Analysis of CD15
444 expression on the surface of intratumor neutrophils (Pillay et al., 2013) revealed two distinct
445 neutrophil populations identified by high and low levels of CD15 (referred to as CD15^{high} and
446 CD15^{low}, respectively, Figure Supp. 1D). Despite being overall similar in NAT, CD15^{high}
447 neutrophils were enriched in tumors in a fraction of patients (Figure Supp. 1E). Thus, based
448 on the CD15^{high} and CD15^{low} neutrophil populations, we divided our cohort in 2 groups,
449 namely low (LN) and high CD15^{high} (HN) neutrophils (Figures 1C and D).
450 In line with previous studies, our data suggested that CD15^{high} neutrophils, which
451 predominantly infiltrate HN tumors, were in a N2-like tumor-promoting functional state
452 (Fridlender et al., 2009). Indeed, we reported that CXCR2^{+}CXCR4^{+} double positive cells

453 were significantly higher in the CD15^{high} compared to the CD15^{low} neutrophil compartment
454 (Figure 1E). Accordingly, HN tumors showed increased frequencies of N2-like tumor-
455 promoting CXCR2^{+}CXCR4^{+} neutrophils (Figure 1F). In line with a tumor-promoting
456 phenotype, CD15^{high} neutrophils expressed significantly higher levels of CD10, a cell surface
457 marker that was proposed to distinguish T-cell suppressive from T-cell stimulatory
458 neutrophils (Figure Supp. 1F) (Fridlender et al., 2009; Marini et al., 2017). Moreover,
459 exposure of neutrophils to interstitial fluid from HN tumors induced higher production of total
460 reactive oxygen (tROS) species (Figure Supp. 1I). Of note, the frequencies of
461 CXCR4^{+}CXCR2^{-} neutrophils, previously defined as aged (Jaillon et al., 2020a), were
462 comparable between CD15^{high} and CD15^{low} neutrophils as well as in HN and LN tumors
463 (Figures Supp. 1G-H). Overall, these data revealed that CRC patients can be stratified
464 based on the abundance of a CD15^{high} neutrophil population, which might have tumor
465 promoting functions.
466 Neutrophil homeostasis in peripheral tissues results from the balance between clearance by
467 macrophages and recirculation regulated by soluble factors (Cox et al., 1995; Grigg et al.,
468 1991) (Buckley et al., 2006; Robertson et al., 2014; Wang et al., 2017; Woodfin et al., 2011).
469 Indeed, frequency of macrophages anticorrelated with CD15^{high} neutrophils (Figure Supp.
470 1J) and was significantly lower in HN compared to LN (Figure Supp. 1K), suggesting that
471 lower clearance in HN tumors might contribute to higher abundance of neutrophils, as
472 previously reported (Peng et al., 2021a).
473 Next, we asked which was the contribution of soluble chemoattractants in determining the
474 CD15^{high} neutrophil difference between HN and LN. This was tested on a microfluidic device
475 that enabled measurement of the ability of freshly isolated neutrophils to migrate through a
476 3D collagen matrix. Surprisingly, migration was higher when neutrophils were exposed to
477 LN compared to HN tumor interstitial fluids (Figures 1G), suggesting that the higher CD15^{high}
478 neutrophils observed in HN compared to LN did not reflect an increase in their recruitment

479 into the TME. On the contrary, exposure of neutrophils to interstitial fluid from HN tumors
480 increased expression of CD15 when compared to LN (Figures Supp. 1L), suggesting an
481 active role of the TME in driving neutrophil function. Therefore, we profiled 49 inflammatory
482 soluble factors in the interstitial fluid of T and NAT from CRC patients, of which 33 gave
483 consistently measurable results (Figure 1H). While not significantly associated neither with
484 demographics nor tumor grade, we found out that a subset of these factors was directly
485 correlated with the frequency of $CD15^{high}$ neutrophils (Figure 1I). In particular, $CD15^{high}$
486 neutrophils were positively correlated with IL-17E/IL-25, which plays important roles in
487 inflammation occurring in the gut (Caruso et al., 2009; Owyang et al., 2006; Wang et al.,
488 2014), it has been shown to upregulate the expression of CXCL1 and CXCL10 (Senra et al.,
489 2019) and promotes a Th2-like responses by inducing IL-4, IL-5 and IL-13 expression (Fort
490 et al., 2001). In agreement, we found that CXCL1, CXCL10, IL-4 and IL-13 were positively
491 correlated with $CD15^{high}$ neutrophils. Interestingly, IL-4/IL-13–stimulated neutrophils have
492 been reported to have diminished ability to form NETs and migrate toward CXCL8
493 (Impellizzieri et al., 2019), suggesting that neutrophils from HN and LN might be functionally
494 different. Enrichment of G-CSF and IL-10 in HN further supported the role of the TME in
495 driving neutrophil polarization toward N2-like functional state (Ferrante; Fridlender et al.,
496 2009; Gerlini et al., 2004; Gholamin et al., 2009; Joshita et al., 2009; Kyo et al., 2000; Moore
497 et al., 2001). Among the detected factors, CXCL12/SDF-1 (from now on referred to as SDF-
498 1) was of particular interest because of its role in neutrophil trafficking and retention at
499 inflammatory site through its binding to CXCR4 (C et al., 2003; Filippo and Rankin, 2018),
500 which we found to be highly expressed on $CD15^{high}$ neutrophils together with CXCR2
501 (Figures 1E-F). Imaging analysis confirmed that overall levels of SDF-1 were higher in HN
502 compared to LN tumors and this was due to the combination of a larger number of αSMA^{+}
503 cancer associated fibroblasts in HN and their higher expression of SDF-1 (Figure Supp.1M-
504 N).

505 Despite surface expression of CXCR4, SDF-1 treatment did not foster neutrophil's migration
506 *in vitro.* On the contrary, IL-8 and CXCL6, well-known chemo-attractants found to negatively
507 correlate with CD15^{high} TANs *in vivo*, showed a pro-migratory effect (Figures Supp. 1O-P).
508 On the other hand, neutrophils treated *in vitro* with SDF-1 showed higher frequency
509 CXCR2^{+}CXCR4^{+} double positive cells (Figures 1J and Supp. 1Q-R), an elevated level of
510 total ROS (Figure 1K), produced more gelatinase (Figure 1L) and adhered more to micro-
511 endothelial cells compared to untreated controls (Figure 1M), which recapitulates, at least
512 in part, *in vivo* observations. The slight increase in CD62L upon SDF-1 treatment supported
513 the idea that these neutrophils were not aged (Figure Supp.1S) (Peng et al., 2021b). In
514 summary, these results showed that tumor infiltration of CD15^{high} neutrophils distinguished
515 between LN and HN patients, and suggested that elevated concentrations of SDF-1
516 changed neutrophil functional state rather than their recruitment.
517
518 **The TME of CRC is infiltrated by two main CD8^{+} T cell populations identified by**
519 **differential expression of CD39 and GZMK.**
520 We next hypothesized that the different abundance of CD15^{high} neutrophils might alter the
521 immune landscape in CRC TME and, in particular, CD8^{+} T cells. CD8^{+} T cell infiltration is
522 unanimously accepted as a favorable prognostic marker in CRC (Chiba et al., 2004; Galon
523 et al., 2014; Naito et al., 1998; Pagès et al., 2009b; Prall et al., 2004; Zlobec et al., 2010).
524 However, querying the collection of non-metastatic CRC patients in the TCGA database with
525 a cytolytic CD8^{+} T cell transcriptional signature did not result in an effective stratification
526 (DFS, p=0.12 Figure Supp. 2A), suggesting that other factors might influence CD8^{+} T cell-
527 mediated response and contribute to determining the clinical outcome. Therefore, we
528 employed high dimensional flow cytometry to carry out a detailed assessment of the diversity
529 in the CD8^{+} T cell compartment, including markers of memory and effector differentiation
530 (CD45RA, CCR7, CD27, CD28, CD127, CX3CR1, CD161), activation (OX40, CD25, HLA-

531 DR), inhibitory receptors (PD1 and TIGIT), tissue residency and tumor reactivity (CD69,
532 CD103 and CD39) and effector molecules (GZMB and GZMK). The whole list is reported in
533 Table 2. Within the TME, $CD3^+$ T cells represented over 60% of the immune infiltrate (Figure
534 Supp 2B) and were enriched in T compared to NAT across patients (Figure 2A). In the T,
535 the composition of the $CD3^+$ T cells included $CD4^+$ Th (T_{Th}) cells, $CD8^+$ T cells, T regulatory
536 (T_{Reg}) cells and T gamma-delta (Tγδ) cells, with $CD4^+$ Th and $CD8^+$ T cells being
537 predominant (Figure 2B).
538 Focusing on the $CD8^+$ T cell compartment, naive (T_N identified by $CD45RA^+CCR7^+$) and
539 central memory (T_{CM} identified by $CD45RA^-CCR7^+$) $CD8^+$ T cells were rare both in the T and
540 in NAT compared to PB (Figure Supp. 2C). In line with previous reports (Pagès et al.,
541 2009b), the majority (about 80%) of the infiltrating $CD8^+$ T cells were effector memory cells
542 (T_{EM}), characterized by $CCR7^-CD45RA^-$ expression (Figures 2C and Supp. 2C). Therefore,
543 based on differential CD27 and CD28 expression (Figure Supp. 2D), we further divided the
544 T_{EM} into 4 phenotypically and functionally distinct subpopulations called EM_1 ($CD27^+CD28^+$),
545 EM_2 ($CD27^+CD28^-$), EM_3 ($CD27^-CD28^-$) and EM_4 ($CD27^-CD28^+$) (Romero et al., 2007). The
546 T_{EM3} and T_{EM4} T cell compartment, which represented effector-like and memory-like
547 phenotypes respectively, were the most represented in T (Figures 2D). We detected low
548 frequencies of terminally differentiated effector memory cells re-expressing CD45RA (T_{EMRA})
549 (Figures 2C and Supp. 2C), a phenotype associated with terminal T cell differentiation
550 (Thome and Farber, 2015). In accordance, only a minority of $CD8^+$ T cells exhibited traits
551 that have been previously associated with “T cell exhaustion” (McLane et al., 2019), such
552 as co-expression of PD-1, LAG3 and TIM3 (Figure Supp. 2E).
553 Analysis with t-distributed stochastic neighbor embedding (tSNE) confirmed that $CD8^+$ T cell
554 profiles were substantially different in the PB, NAT and T compartments also at single-cell
555 level (Figures 2E-F), independently from other factors like patient's age, gender or tumor
556 stage (Figure 2G). Based on the calculated mean fluorescence intensity (MFI) and

557 frequency of different markers (Figures Supp. 2F-G), we identified 20 different clusters (CL)
558 in the $CD8^+$ T cell compartment (Figures Supp. 2G-H, CL 9 and 16 were excluded from
559 further analyses because their frequencies were below 0.5%). A number of clusters were
560 enriched in PB compared to NAT and T and were characterized by lack of expression of
561 residency and activation markers (CD69, CD103 and CD39). These included: CL3 -
562 annotated as naïve (T_N) and characterized by high levels of CD45RA, CCR7 and CD127
563 expression and lack of activation markers; CL1, 5 and 18 were annotated as T_{EMRA} being
564 characterized by low CCR7 level, general lack of expression of memory markers along with
565 high levels of the cytolytic molecule GRZB; CL6 - annotated as central memory (T_{CM})
566 because of the expression of several memory-associated markers (CCR7, CD127, CD27,
567 CD28) but absence of activation and cytotoxic markers (Figures 2H and Supp. 2G). Four
568 other clusters, instead, were enriched in T and NAT compared to PB, indicating that they
569 were tissue-infiltrating $CD8^+$ T cell subsets. These were: CL14 and 20 mainly composed by
570 $CD45RA^{neg}CCR7^{neg}CD28^{high}CD27^{low}CX3CR1^{pos}$ T_{EM} cells, and CL8 and 11 annotated as
571 tissue-resident memory T cells (T_{RM}) since they displayed high expression of markers of
572 memory (CD127 and CD28) and tissue residency (CD69 and CD103). These two tissue-
573 infiltrating T_{RM} subsets expressed intermediate levels of CD161 and were mostly present in
574 NAT (Figures 2F and Supp. 2G). In line with previous reports (Fergusson et al., 2015), this
575 population appeared to be different from the $CD161^{high}$ mucosal associated invariant T cells
576 (MAIT) in CL19, which appeared to be equally represented in all three different
577 compartments in early CRC patients.
578 We next focused on CL12 and CL4, which were specifically enriched in T compared to NAT
579 and PB, and found that they were mainly composed by a T cell population reminiscent of
580 $CD8^+$ T_{EM} cells ($CD45RA^{low}CCR7^{low}CD28^{int}CD27^{low}CD8^+$). They showed low or intermediate
581 levels of CD127 and CX3CR1, and differential expression of activation, exhaustion and
582 cytotoxicity markers (Figures 2H and Supp. 2G). In particular, CL12 identified $CD8^+$ T cells

583 with negligible expression of GZMK and high levels of CD39, a marker that has been
584 recently associated with tumor antigen encounters (Duhen et al., 2018; Simoni et al., 2018).
585 On the contrary, CL4 was primarily composed by $CD8^+$ T cells characterized by lack of CD39
586 and elevated levels of GZMK (Figure 2I). Collectively, these data showed that CRC TME is
587 mainly infiltrated by two distinct $CD8^+$ T_{EM} cells populations that could be distinguished
588 based on GZMK and CD39 expression ($GrzK^{high}CD39^{neg}$ and $GrzK^{low}CD39^{pos}$).
589 Using a manual gating strategy, we observed that $CD8^+$ T_{EM} compartment was
590 predominantly occupied by $CD39^{neg}$ T cells (Figure 3A). However, the expression of CD69
591 and CD103 in the $CD39^{neg}$ $CD8^+$ T_{EM} cells indicated that they were not derived from blood
592 contamination (Figures Supp. 3A-B). Thus, we decided to focus our attention on the
593 characterization of this newly emerged population of $CD8^+$ T_{EM}, annotated as CL4 and
594 identified by the unique expression of CD39 and GZMK. Manual gating analysis showed
595 that $GZMK^{high}$ $CD8^+$ T_{EM} cells were almost entirely $CD39^{neg}$ (Figure 3B) and were
596 characterized by significantly lower expression of PD1 and higher GZMB when compared
597 to their $GZMK^{low}$ counterpart (Figure 3C). When FACS-sorted based on CD39 expression
598 and assessed for their ability to produce effector molecules, $CD39^{neg}$ $CD8^+$ T cells produced
599 significantly higher levels of GZMK and retained the ability to produce IFNγ, TNFα and
600 GZMβ compared to their $CD39^{high}$ counterparts (Figure Supp. 3D). In conclusion, we
601 reported that the TME in early-CRC patients was highly infiltrated by a novel $GZMK^{high}$ $CD8^+$
602 T_{EM} population, which lacked CD39 expression and was distinct from the "exhausted-like"
603 $GZMK^+$ $CD8^+$ T cell subpopulations recently reported by others (Hornburg et al., 2021;
604 Mogilenko et al., 2021; Zhang et al., 2018).
605

606 **Neutrophils modulate CRC infiltrating $CD8^+$ T cells increasing their GZMK expression.**
607 Neutrophils influence $CD8^+$ T cell responses both in animal models and humans. However,
608 evidences are still sparse and often contrasting (Eruslanov et al., 2014; Jaillon et al., 2020a;

609 Li et al., 2020; Sangaletti et al., 2014a), and even the stratification of non-metastatic CRC
610 patients in the TCGA database was not effective when combining neutrophils to the cytolytic
611 $CD8^+$ T cell transcriptional signature (Figure Supp. 4A, p=0.44). Thus, since CRC patients
612 can be distinguished in two distinct subgroups based on the abundance of $CD15^{high}$
613 neutrophils, we sought to better understand their link with $CD8^+$ T cells. Strikingly, Spearman
614 correlation analysis revealed that frequencies of intra-tumor $CD15^{high}$ neutrophils were
615 positively correlated with frequencies of $GZMK^{high}$ $CD8^+$ T_{EM} cells (Figure 4A). Of note, no
616 significant correlation was found between $CD15^{high}$ neutrophils and other $CD8^+$ T cell
617 differentiation states or activation markers (Figures Supp. 4B and C). Since $CD4^+$ T cells
618 were the predominant population in the $CD3^+$ T cell compartment, we sought to address
619 their potential contribution to GZMK production. Our data showed that $CD4^+$ T cells
620 produced low amounts of GZMK and they were neither correlated with $CD15^{high}$ neutrophils
621 abundance nor differentially present in the TME of HN and LN (Figures Supp. 4D-F).
622 Together, these data prompted us to investigate the specific cross-talk between $CD15^{high}$
623 neutrophils and $GZMK^{high}$ $CD8^+$ T_{EM} cells.
624 Despite comparable frequencies of $GZMK^{high}$ $CD8^+$ T_{EM} cells in NAT and PB of LN and HN
625 patients (Figure Supp. 4G), intratumor $CD8^+$ T_{EM} cells expressed higher levels of GZMK in
626 HN compared to LN patients, as assessed both by FACS (Figure 4B-C) and quantitative
627 confocal microscopy (Figure 4D), confirming that the higher proportion of $GZMK^{high}$ $CD8^+$
628 T_{EM} cells was a tumor-specific hallmark in HN CRC patients.
629 Next, we investigated if neutrophils were directly involved in inducing a $GZMK^{high}$ phenotype.
630 In CRC patients, $CD8^+$ T cells in proximity to neutrophils (distance r ≤10um) expressed
631 higher GZMK levels compared to other cell types (Figure 4E), suggesting that the interaction
632 might be contact-mediated and the effect direct. Indeed, co-culturing of optimally activated
633 $CD8^+$ T cells and neutrophils derived from healthy donors demonstrated that the frequency
634 of $GZMK^{high}$ $CD8^+$ T cells increased in presence of neutrophils and this was dependent from

635 both the ratio of the two cell types and their physical contact (Figure 4F). These data
636 revealed that skewing of $CD8^+$ T cells toward a $GZMK^{high}$ phenotype resulted from direct
637 cross-talk between neutrophils and $CD8^+$ T cells at the tumor site.
638
639 **$GZMK^{high}$ $CD8^+$ T_{EM} cells promote relapse in early CRC.**
640 To gain insight into the contribution of $GZMK^{high}$ $CD8^+$ T_{EM} and their interaction with
641 neutrophils to the anti-tumor response in CRC, we analyzed the immune infiltrate during
642 tumor progression in the syngeneic MC38 mouse model of colon cancer (Corbett et al.,
643 1975). Similarly to what we observed on CRC patients, intratumor $GZMK^{high}$ $CD8^+$ T cells
644 were positively correlated with the percentage of intratumor neutrophils (defined as
645 $CD11b^+Ly6g^+CXCR2^+$) in the MC38 model (Figure 4G). In addition, murine $CD8^+$ T cells
646 increased GZMK expression upon co-culturing with neutrophils from bone marrow and, to a
647 larger extent, with tumor-infiltrating neutrophils (Figures 4H). Finally, the frequencies of
648 intratumor $GZMK^{high}$ $CD8^+$ T cells and tumor-infiltrating neutrophils were positively
649 correlated with the size of tumors (Figures 4I). Overall, these results confirmed the existence
650 of a cross-talk between neutrophils and $CD8^+$ T cells resulting in an increased GZMK
651 production, and supported a model where $GZMK^{high}$ $CD8^+$ T cells might foster tumor
652 progression.
653 Emerging evidence suggests that GZMK might promote inflammation and untargeted tissue
654 damage (Wensink et al., 2015). This has been related to the activity of GZMK as an
655 extracellular protease and its ability to promote epithelial-to-mesenchymal transition (EMT)
656 by remodeling components of the extracellular matrix (Bouwman et al., 2021). We tested
657 this hypothesis *in vitro* by exposing a functional human intestinal epithelial model to the
658 neutrophils-$CD8^+$ T cells co-culture, which we showed to induce GZMK production by $CD8^+$
659 T cells. Compared to each of the two cell types alone, the co-culture induced a significant
660 decrease in E-Cadherin expression (Figure 4J), a feature associated to EMT and tumor

661 malignancy (MA et al., 2005; Zeisberg and Neilson, 2009). Similar results were obtained
662 when the intestinal epithelial model was treated with purified GZMK (Figure 4K), providing
663 evidence that release of GZMK would be sufficient to induce tissue remodeling. In line with
664 this, HN CRC tumors showed reduced expression of E-Cadherin compared to LN (Figure
665 4L), suggesting that infiltration of GZMK^{high} CD8^{+} T cells could be linked to tumor
666 progression and, possibly, contribute to relapse.
667 To test this link, we profiled patients in our cohort that encountered early relapse (Rel, n=5)
668 and we observed that frequencies of CD15^{high} neutrophils and GZMK^{high} CD8^{+} T_{EM} cells in
669 their T were comparable to HN and significantly higher than LN (Figure 5A-B). In agreement,
670 T from relapsed patients were enriched in CL4 (mainly composed of CD8^{+} T_{EM}
671 GZMK^{high}CD39^{neg}), while CL12 (mostly CD8^{+} T_{EFF} GZMK^{low} CD39^{pos}) was poorly
672 represented (Figures 1H-I and 5C-E). All together, these results support the existence of a
673 CD8-neutrophil crosstalk at the tumor site, which significantly contributes to the clinical
674 outcome (Pagès et al., 2009b, 2009c). Thus, evaluation of the different subtypes of cytotoxic
675 CD8^{+} T cells could provide a mean to predict tumor recurrence and patient survival.
676
677 **GZMK expression correlates with a distinct transcriptional program in CD8^{+} T_{EM}.**
678 Aiming to build a signature that could address the prognostic potential of infiltrating
679 GZMK^{high}CD8^{+} T_{EM} cells, paired T and NAT tissues from 8 CRC (stage I-III) HN patients
680 were profiled by single cell RNA sequencing (scRNAseq). We collected data from a total of
681 52316 cells. Mean reads per cell were 94183 (min:37500; max:235694) with a median
682 number of genes detected per cell of 3779 (min:1433; max:5392). Sequencing saturation
683 was >49% for all samples, indicating comprehensive sampling of the available transcripts.
684 After processing and normalization, dimensionality reduction was performed with uniform
685 manifold approximation and projection (UMAP). Shared nearest neighbor (SNN) clustering
686 distinguished eleven different clusters that were annotated to nine broad cell lineages,

687 including epithelial (*EPCAM*$^+$), endothelial (*CD34*$^+$), mesenchymal (*MMP2*$^+$), B cells
688 (*MZB1*$^+$), and T/NK (*CD3D*$^+$) (Figures Supp. 5A-C). Notwithstanding the expected variability
689 among patients, all the annotated clusters were represented across the patients (Figure
690 Supp. 5D). Expression analysis across all the annotated cell subtypes highlighted the T/NK
691 cluster as the main source of *GZMK* expression in the TME of HN (Figure Supp. 5E).
692 Zooming in on the 8523 cells composing the T/NK cluster, we generated a new UMAP that
693 further distinguished seven T cell subtypes (Figure Supp. 5F), among which cluster 1 was
694 enriched in CD4$^+$ while clusters 3 and 4 were enriched in CD8$^+$ T cells (Figures Supp. 5G-
695 H). Interestingly, *GZMK* expressing cells were mostly restricted to the CD8$^+$ clusters 3 and
696 4, confirming results from our phenotypic analysis. Within the CD8$^+$-enriched T cells clusters
697 3 and 4, we could identify eleven sub-clusters (Figures 6A). These clusters were annotated
698 with manually curated gene-sets (Table Supp. 1) based on recent literature (Li et al., 2019).
699 While confirming the presence of previously described putative T cell sub-populations, this
700 analysis highlighted a remarkable transcriptional heterogeneity. The eleven clusters
701 included minor fractions of CD4$^+$ T cells falling in the memory (CD4_T_{EM}), the *FOXP3*
702 expressing regulatory (Treg), *CD40LG* positive mucosal associated invariant T (MAIT) and
703 exhausted (Tex) T cell clusters. Co-expression of *TRDC* and *TRGC1* enabled discrimination
704 of gamma delta T cells (Tγδ), while higher expression of *AKR1C3*, *CXC3R1*, *FCER1G*,
705 *NKG7* and *PRF1* were distinctive transcriptional traits of the natural killer (NK) cluster. Naive-
706 like T cells were assigned based on expression of *IL7R*, *CCR7* and *SELL* signature genes
707 (Figures Supp. 6A and C). Most of the retrieved T cells fell within the CD8$^+$ T effector memory
708 subgroup (CD8_T_{EM}, Figure Supp. 6B) characterized by low expression of *GZMB* and high
709 expression of *GZMK* (Figures 6B), in agreement with the GZMK^{high} T cells identified by
710 FACS analysis. On the other hand, marginal expression of genes associated to exhaustion,
711 such as *CTLA-4*, *PDCD-1*, *CXCL13*, *HAVCR2*, *ENTPD1* and *LAYN*, and differential
712 expression analysis revealed that CD8_T_{EM} were considerably distinct from T_{EX} cells

713 (Figures 6C-D). In addition, pseudotime analysis showed that CD8_T_{EM} were closer to
714 Naive-like T cells than to terminally differentiated effectors (T_{TE}, Figures 6E and Supp. 6D).
715 The borders between CD8_T_{EM} and the clusters labeled as CD8_T_{EM}-PD1 and HLADR_CD8
716 were diffuse, instead, even though hierarchical clustering of differentially expressed genes
717 confirmed the robustness of the model. While suggesting that transcriptional gradients may
718 contribute to T cell heterogeneity, this observation also marks intermediate states on the
719 transition of CD8_T_{EM} toward exhaustion, for example, through the expression of genes like
720 *PDCD1* and *CXCL13*. Functionally, pathway enrichment analysis indicated that, despite
721 having lower cytolytic potential (padj= 0.005) compared to T_{TE} and NK cells, both CD8_T_{EM}
722 and HLADR_CD8 (both expressing high levels of *GZMK* levels) were not impaired in
723 proliferation (Figure Supp. 6E). In particular, CD8_T_{EM} had lower expression of lymphocyte
724 activation and migration and higher cell-cell adhesion signatures (Figure Supp. 6E).
725 Noteworthy, similar expression levels of effector molecule *TNFα* characterized the two
726 subsets of CD8_T_{EM} grouped based on *GZMK* expression (Figures Supp. 6F-G), further
727 supporting that *GZMK* expression is not associated with a dysfunctional state in CD8_T_{EM}
728 (see also Figure Supp. 3D). Finally, querying of publicly available CRC datasets on The
729 Cancer Genome Atlas (TCGA) using a transcriptional signature that distinguished CD8_T_{EM}
730 highly expressing *GZMK* among those defined by scRNAseq (Figure Supp. 6I, see Methods
731 for details), showed better prognosis in patients with lower infiltration of CD8 T_{EM} expressing
732 high *GZMK* (Figure 6G). This signature provided a better prognostic value than the
733 functional signature related to the cytolytic activity of $CD8^+$ T cells and it was effective in
734 stratifying patients with other carcinoma types, like the TCGA lung adenocarcinoma (Figure
735 Supp. 6J).
736 In conclusion, our functional and transcriptional characterization of the tumor immune
737 infiltrates resulted in an effective stratification of patients and predicted a different risk of

738 relapse in early-stage CRC patients. Our findings have the potential to be extended to other
739 cancer types, including lung carcinoma.
740
741
742 **DISCUSSION**
743 We conducted unbiased analysis of the immune cells within and across CRC patients by
744 combining multiparametric flow cytometry with functional assays and single cell
745 transcriptomics. Our data reveal that CRC patients can be stratified based on high (HN) or
746 low (LN) $CD15^{high}$ neutrophil infiltration and highlight the emergence of a novel $GZMK^{high}$
747 $CD8^{+}$ T_{EM} cell population as a hallmark of HN tumors (Figure 7). The predominance of the
748 $GZMK^{high}$ $CD8^{+}$ T_{EM} cells in CRC patients that encountered an early relapse and the
749 correlation with poor clinical outcome on an independent cohort underline the clinical
750 relevance of the cell population and its therapeutic potential.
751 Despite several attempts to profile the immune cell content of CRC (Pagès et al., 2009b;
752 Zhang et al., 2018), the prognostic value of immune cell infiltration is not conclusive,
753 especially regarding neutrophils (Shaul and Fridlender, 2019). We provide evidence that
754 neutrophils are the most abundant innate cell population infiltrating the tumor bed in early-
755 stage CRC. Pro-tumorigenic roles have been ascribed to neutrophils across different tumor
756 types (Galdiero et al., 2018; Mantovani et al., 2011), including promotion of angiogenesis
757 and immunosuppression (Bronte et al., 2016; Coffelt et al., 2016), but it is not clear whether
758 distinct neutrophil populations gather the tumor or if phenotypic changes occur inside the
759 TME. The presented analysis of the canonical neutrophil marker CD15 (Pillay et al., 2013)
760 reveals phenotypic changes specifically in the population associated with tumors. Intratumor
761 neutrophils from LN patients have significantly lower expression of CD15 compared to
762 healthy- and patient-derived peripheral neutrophils. Conversely, neutrophils infiltrating the
763 TME of HN patients maintain high levels of CD15 expression, are enriched in

764 CXCR2^{+}CXCR4^{+} cells and tend to produce more ROS, in line with a so called N2-like tumor-
765 promoting functional state (Fridlender et al., 2009). Interestingly, treatment of freshly
766 isolated neutrophils with interstitial fluid from HN tumors led to higher CD15 expression but,
767 differently from interstitial fluid from LN, did not foster migration, suggesting that specific
768 soluble factors in the TME might polarize neutrophils toward a CD15^{high} state rather than
769 increasing their recruitment. Neutrophils are recruited early to the site of inflammation, where
770 their not-specific antimicrobial functions can endanger the integrity of the host tissue in case
771 of inappropriate retention (Nathan and Ding, 2010; Rock et al., 2010). To avoid it, in addition
772 to clearance by macrophages-directed efferocytosis (Cox et al., 1995; Grigg et al., 1991),
773 neutrophils redistribute into surrounding tissues or vasculature through reverse migration
774 (Buckley et al., 2006; Robertson et al., 2014; Wang et al., 2017; Woodfin et al., 2011), which
775 has been suggested to follow desensitization to local chemotactic gradients (Holmes et al.,
776 2012; Powell et al., 2017; Robertson et al., 2014). In this regard, SDF-1/CXCR4 signaling
777 plays an important role in the retention of neutrophils at inflammatory sites (Isles et al.,
778 2019). Since clearance by resident tissue macrophages has been associated with reduction
779 of CD15 surface expression on neutrophils (Shelley et al., 2018), we can speculate that the
780 enrichment of CD15^{high} neutrophils in HN tumors might be due, at least in part, to inefficient
781 clearance, as previously demonstrated in other tumor contexts (Peng et al., 2021a). On the
782 other hand, our analysis of differentially abundant soluble factors pointed at SDF-1, which
783 correlates *in vivo* with frequency of CD15^{high} neutrophils and, *in vitro,* increased adhesion
784 and release of TME's remodeling factors rather than driving chemotaxis. Overall, these data
785 suggest that elevated concentrations of SDF-1 may promote the reprogramming of
786 neutrophils infiltrating HN tumors. Future studies would need to address if this may lead to
787 an increased retention of neutrophils in the tumor, altering their homeostatic turnover.
788 Neutrophils influence CD8^{+} T cell-mediated responses both in animal models and humans.
789 However, results are still sparse and often conflicting (Eruslanov et al., 2014; Governa et

790 al., 2017; Jaillon et al., 2020b; Li et al., 2020; Sangaletti et al., 2014b; Singhal et al., 2016;
791 Wu et al., 2014). We provide evidence that direct interaction between neutrophils and $CD8^+$
792 T cells leads to increased GZMK expression, both *in vivo* and *in vitro*. When compared to
793 their $GZMK^{neg}$ counterpart, $GZMK^{high}$ $CD8^+$ T_{EM} cells harbor significantly lower PD-1
794 expression and higher levels of Gzmβ, posing these cells as distinct compared to the $GZMK^+$
795 $CD8^+$ T cell subpopulations previously identified and described as pre-dysfunctional (Guo et
796 al., 2018; Hornburg et al., 2021; Mogilenko et al., 2021; Zhang et al., 2018). Moreover, their
797 abundance in the TME is independent from tumor stage and aging ($P > 0.05$, ANOVA)
798 (Mogilenko et al., 2021). Of particular relevance, $GZMK^{high}$ $CD8^+$ T_{EM} cells lack CD39
799 expression, which might suggest that they are contributing to a general inflammatory state
800 (Chiou et al., 2021; Corridoni et al., 2020) rather than targeting specifically tumor associated
801 antigens (Scheper et al., 2019; Simoni et al., 2018). Thus, the high proportion of $GZMK^{high}$
802 $CD39^{neg}$ $CD8^+$ T_{EM} cells found in HN CRC patients raises the possibility that they could be
803 involved in a cross-reactive response, favoring cancer progression. The alloreactive-like
804 transcriptional signature associated with $GZMK^{high}$ $CD8^+$ T_{EM} favors this model, with
805 upregulation of CRTAM and CCL5/RANTES promoting retention of activated $GZMK^{high}$
806 $CD8^+$ T_{EM} cells (Arase et al., 2005; Cortez et al., 2014; Galibert et al., 2005) and recruitment
807 and immunosuppressive polarization of myeloid cells (Aldinucci et al., 2020; Schall et al.,
808 1990; Seo et al., 2020; Swanson et al., 2002; Walzer et al., 2003), respectively. However,
809 only future analysis of the TCR clonality of $GZMK^{high}$ $CD39^{neg}$ $CD8^+$ T_{EM} will allow testing
810 this hypothesis unequivocally.
811 We show that, at least in HN CRC patients, $CD8^+$ T_{EM} are the main source of GZMK. Further
812 studies are needed to determine whether $CD8^+$ T cells recruited to the tumor are skewed by
813 neutrophils toward a $GZMK^{high}$ phenotype or, conversely, the presence of $GZMK^{high}$ $CD8^+$ T
814 cells impacts neutrophil homeostasis and function, as already proved for other immune cell
815 populations (Joeckel et al., 2011). Regardless of the order of events, GZMK might play a

816 pathogenic role by contributing to inflammation and tissue damage. This relates to its non-
817 cytotoxic activity as extracellular protease and its ability to promote cellular migration and
818 epithelial-to-mesenchymal transition (EMT) by remodeling components of the extracellular
819 matrix (Joeckel and Bird, 2014; Wensink et al., 2015), facilitating cytokine responses (M et
820 al., 2016; Wensink et al., 2014) In line with this, HN tumors showed reduced expression of
821 E-Cadherin compared to LN, which is a feature of EMT and tumor malignancy. Along with
822 tangible therapeutic implications for future interventions, high expression of GZMK by
823 infiltrating $CD8^+$ T_{EM} in response to $CD15^{high}$ neutrophils links them to tumor progression
824 rather than anti-tumor function, suggesting that integrating functional information resulting
825 from the crosstalk of $CD8^+$ T cells with different components of the immune contexture and
826 the stroma might implement the prognostic value of current biomarkers, which are mostly
827 based on limited phenotypic or transcriptional $CD8^+$ T cell characteristics.
828
829
830 **LIST OF ABBREVIATIONS**
831 Colorectal Cancer (CRC)
832 Granzyme K (GZMK)
833 Stromal Cell-Derived Factor 1 (CXCL12/SDF-1)
834 Tumor-Node-Metastasis (TNM)
835 Tumor Microenvironment (TME)
836 Tumor Infiltrating Lymphocytes (Tils)
837 Peripheral Blood (PB)
838 Tumor (T)
839 Normal Adjacent Tissue (NAT)
840 Dendritic Cells (DCs)
841 High $CD15^{high}$ Neutrophils (HN)

842 Low CD15^{high} Neutrophils (LN)

843 Total Reactive Oxygen Species (TRos)

844 CD4^{+} Th Cells (T_{th})

845 T Regulatory Cells (T_{reg})

846 T Gamma-Delta Cells (Tγδ)

847 Naive T Cells (T_N)

848 Central Memory T Cells (T_{CM})

849 Effector Memory T Cells (T_{EM})

850 Terminally Differentiated Effector Memory T Cells Re-Expressing CD45RA (T_{EMRA})

851 T-Distributed Stochastic Neighbor Embedding (Tsne)

852 Mean Fluorescence Intensity (MFI)

853 Clusters (CL)

854 Tissue-Resident Memory T Cells (T_{RM})

855 Mucosal Associated Invariant T Cells (MAIT)

856 Epithelial-To-Mesenchymal Transition (EMT)

857 Early Relapse (Rel)

858 Single Cell RNA Sequencing (scRNAseq)

859 Uniform Manifold Approximation And Projection (UMAP)

860 Shared Nearest Neighbor (SNN)

861 Exhausted T Cells (T_{ex})

862 Natural Killer Cells (NK)

863 Terminally Differentiated Effectors Cells (T_{TE})

864 The Cancer Genome Atlas (TCGA)

865 Peripheral Blood Mononuclear Cells (PBMCs)

866 Polymorphonuclear Leukocytes (PMNs)

867 Trans-Epithelial Electrical Resistance (TEER)

868 CACO2

869 Human Micro-Endothelial Cells (HMEC1)

870 Integrated MFI (Imfi)

871 Immunohistochemistry (IHC)

872 Formalin-Fixed Paraffin Embedded (FFPE)

873 Unique Molecular Identifiers (UMI)

874 Single Cell Mouse Cell Atlas (SCMCA)

875 Overall Survival (OS)

876 Disease-Free Survival (DFS)

877 Colon Adenocarcinoma Cohort (COAD)

878

879

880 **FIGURE LEGENDS**

881 **Figure 1. Early-stage colorectal cancer (CRC) patients can be stratified based on the**
882 **abundance of CD15^{high} neutrophils in the tumor microenvironment (TME). A.** Study
883 design. Immune analysis of Tumor tissues (T), Normal Adjacent Tissues (NAT) (10 cm from
884 T) and Peripheral Blood (PB) of early-stage CRC patients (n=42). **B.** Frequency of Tumor
885 Associated Neutrophils (TAN) defined as CD45^{+} CD11b^{+} HLADR^{-} CD56^{-} CD66b^{+} within
886 CD45^{+} immune compartment in T compared with NAT samples in CRC patients (total n=22).
887 Bars indicate 90-10 percentile. **C.** Density plot of CD15 expression within TAN defining a
888 bimodal distribution in the CRC cohort of patients. Patients were clustered as low (LN) or
889 high (HN) based on CD15 expression. **D.** Frequency of CD15^{high} neutrophils in LN and HN
890 patients. Bars indicate 90-10 percentile. **E.** Bar plot of CXCR4^{+} CXCR2^{+} cell frequency within
891 CD15^{low} and CD15^{high} neutrophils. **F.** Bar plot of CXCR4^{+} CXCR2^{+} cell frequency within LN
892 and HN neutrophils. **G.** Representative brightfield images of neutrophils migration assay on

893 the microfluidic device. Interstitial Fluid of T and NAT from HN and LN patients were tested.
894 Bar plot of number of migrating neutrophils on chip upon stimulation with IF from HN (N=6)
895 and LN (N=5) patients. Scale bar 100mm. **H.** Heatmap showing the abundance of soluble
896 molecules in from IF of T (tumor, light blue) and NAT (far-tumor, pink) tissues. For all the
897 samples, tissue type, tumor grade, sex, age and Microsatellite Instability (MSI) status are
898 indicated. **I.** Spearman correlation between soluble molecules in T IF and $CD15^{high}$
899 neutrophils. **J.** Frequency of $CXCR4^{+}$ $CXCR2^{+}$ in Healthy Donors (HD) fresh-isolated
900 neutrophils treated with SDF-1. **K.** Bar plot representation of total ROS (tRos) MFI within
901 SDF-1 treated-neutrophils from healthy donors (HD). **L.** Gelatinase activity assay on
902 neutrophils freshly-isolated from HD and treated with SDF-1 for the indicated time. Bar plot
903 representation of fold change over untreated control. **M.** Quantification of adherent
904 neutrophils on endothelial cells after 2 hours treatment with SDF-1.
905
906 **2. High-dimensional single cell analysis of $CD8^{+}$ T cells identifies a tumor-specific**
907 **$CD39^{-}$ $GzmK^{+}$ population enriched in early-stage CRC. A.** CD3 Lymphocytes frequency
908 within $CD45^{+}$ in T compared with NAT. Bars indicate 90-10 percentile. **B-D.** UMAP
909 Representation of concatenated $CD3^{+}$ T cells from T sample with bar plot quantification. **B.**
910 Cytotoxic $CD8^{+}$ T cells (blue), Th $CD4^{+}$ (purple), Treg $CD4^{+}$, $CD25^{+}$, $CD127^{-}$ (pink) and γδT
911 cells (orange) distribution. **C.** Naive T cells (light green), central memory T cells (dark green),
912 effector memory T cells (dark blue), effector memory cells re-expressing CD45RA (light blue)
913 distribution. **D.** effector memory T cells subtypes (EM_{1-4}), see main text for description. **E.**
914 tSNE representation of Phenograph algoritm identified 18 clusters of concatenated CD8+ T
915 cells (3,000 cells/sample) from T (n=34), NAT (n=17) and PB (n = 22) samples from CRC
916 patients. **F.** Cluster representation in different tissues: PB, NAT, T. **G.** Hierarchical
917 metaclustering of CRC patients derived samples based on Phenograph identified clusters

918 using Ward's minimum variance method. For all the samples, sample type, grade, sex, age
919 are indicated. **H.** Balloon plot of the average expression levels and expression frequencies
920 of marker of differentiation, residency, memory, cytotoxicity, tumor reactivity, activation and
921 exhaustion in clusters identified in (E-F) and enriched in T. **I.** Bar plot of $CD39^+$ $GzmK^-$ and
922 $CD39^-$ $GzmK^+$ frequency within Cluster 4 and Cluster 12, respectively. *, P < 0.05**, P < 0.01
923 ***, P < 0.001.
924
925 **Figure 3. Phenotypic characterization of the $CD39^-$ $GZMK^+$ $CD8^+$ T cell population**
926 **infiltrating early stage CRC patients.**
927 **A.** Representative contour plot and quantification of $CD39^-$ and $CD39^+$ frequency within
928 $CD8^+$ T_{EM}. **B.** Representative contour plot and quantification of $CD39^-$ and $CD39^+$ frequency
929 within $GZMK^+$ $CD8^+$ T_{EM}. **C.** Bar plot showing frequencies of the indicated markers within
930 $GZMK^+$ (dark blue) and $GZMK^-$ (light gray) $CD8^+$ T_{EM}. ***; P < 0.001.
931
932 **Figure 4. $CD15^{high}$ neutrophil accumulation induces GZMK expression in $CD8^+$ T cells,**
933 **leading to tissue remodeling. A.** Spearman correlation between $CD15^{high}$ neutrophils and
934 expression of GZMK within $CD8^+$ T_{EM} cells on each individual CRC patient (black dots).
935 Shadowed area (dark blue) includes High Neutrophils (HN) patients. **B.** Representative
936 contour plots of $CD8^+$ T_{EM} GZMK expression in Low Neutrophils (LN, turquoise) and High
937 Neutrophils (HN, purple) patients. Percentage of $CD15^{high}$ neutrophils are indicated. **C.** Box
938 plot of $GZMK^+$ $CD8^+$ T_{EM} cells in HN (n=10) and LN (n=6) patients. **D-E**. Representative
939 confocal images and quantification of GZMK Mean Fluorescence Intensity (MFI) in (**D**) HN
940 (n=9) and LN (n=6) tumors. Scale bar 10mm. **(E)** $CD8^+$ and $CD8^-$ cells within a 10 μm

941 distance from neutrophils (CD66b$^+$). Scale bar 5 mm. (See Methods for details). **F.** Co-
942 culture of CD8 and neutrophils isolated from peripheral blood of healthy donors. Bar plot of
943 frequency of GZMK$^+$ within CD8$^+$ T cells after co-culture, in plate or in Transwell (TRANS)
944 with neutrophils derived from healthy donors (HD). Neutrophils-to-CD8$^+$ T cells ratio in the
945 co-cultures are indicated. **G-I.** MC38 tumor bearing mice were euthanized and neutrophils
946 content and GZMK expression in tumors evaluated by flow cytometry. **(G)** Spearman
947 correlation between frequency of GZMK$^+$ within CD8$^+$ T cells and frequency of CXCR2$^+$ cells
948 within Ly6G$^+$ CD11b$^+$ neutrophils in MC38 tumors. **(H)** Bar plot of GZMK$^+$ MFI within
949 activated CD8$^+$ T cells co-cultured in a 1:1 ratio with neutrophils isolated from Bone Marrow
950 (BM) or tumors from MC38 tumor bearing mice. **(I)** Spearman correlation between frequency
951 of GZMK$^+$ within CD8$^+$ T cells in MC38 tumors and tumor size (mm^3). **J-K.** Representative
952 confocal images and quantification of CACO-HT29 cells co-cultured on transwells and then
953 (**J**) exposed for 24h to neutrophils (NEU), CD8$^+$ T cells (CD8) or neutrophils/CD8$^+$ T cells in
954 1:1 ratio (1:1), or (**K**) treated for 24h with control media (CTR) or active recombinant human
955 GzmK (GzmK). Staining for DAPI in blue and E-Cadherin in green. Scale bar 100μm. **L.**
956 Representatives confocal images and quantification of FFPE sections of LN and HN tumors
957 from CRC patients. Staining for DAPI in blue and E-Cadherin in green. Scale bar 50μm.
958

959 **Figure 5. CRC patients encountering early relapse have high infiltration of GZMK$^+$**
960 **CD8$^+$ T effector memory (T_{EM}) cells. A.** Representative histogram and quantification of
961 GZMK frequency within T_{EM} CD8$^+$ Tumor Infiltrating Lymphocytes (TILs) in High Neutrophils
962 (HN), Low Neutrophils (LN) and Early-Relapsed (Rel) patients. **B.** Representative histogram
963 and quantification of CD15^{high} neutrophils in HN, LN, Rel tumors. **C.** Bar plot of Cluster 12
964 (CL12, green) and Cluster 4 (CL4, purple) in HN, LN and Rel tumors. **D.** Representative

965 contour plot of GZMK and CD39 expression within $CD8^+$ T_{EM} in in HN, LN and Rel tumors.

966 **E.** Box plot of $CD39^-$ $GZMK^+$ within $CD8^+$ T_{EM} cells in HN, LN and Rel tumors.

967

968 **Figure 6. Single-cell RNAseq analysis on CRC patients defines an effective**

969 **prognostic signature based on $CD8^+$ $GZMK^+$ T_{EM} abundance.** UMAP projection of $CD8^+$

970 T cells. Colors represent different T cell subtypes. Key genes used for manual annotation

971 are indicated. **B.** Violin plots showing the normalized expression of GZMB and GZMK in the

972 different T $CD8^+$ cell subtypes. **C.** UMAP showing the expression of CD8_Tem and CD8_Tex

973 signatures for each cell. Cells are color coded based on SNN-clustering, dot size reflects

974 the expression of the signature for each cell. **D.** Violin plots showing the expression of genes

975 associated with T-cell exhaustion within the indicated cell subtype. **E.** Monocle pseudotime

976 analysis of the $CD8^+$ T cell subtypes. The pseudotime line connects the indicated T cell

977 subtypes identified in (A). **F.** UMAP as in (C) showing the expression of Cytolysis and

978 Allograft rejection signatures. **G.** Kaplan-Meyer analysis of the association of $GZMK^{high}$ cell

979 subtype' abundance with disease free survival (DFS) on the TCGA-COAD cohort (see

980 Methods and Table Suppl. 1 for details). High signature in red, low in turquoise.

981

982 **Figure 7. Simplified graphical summary.** Abundance of $CD15^{high}$ neutrophils in the tumor

983 identifies High (HN) and Low (LN) neutrophil subgroups of early-stage CRC patients (**1**).

984 Elevated SDF-1 levels in HN tumors reshape the functional state of infiltrating neutrophils

985 (**2**), promoting their retention (**3**) and activation (**4**) at the tumor site. The interaction with

986 neutrophils (**5**) pushes effector memory $CD8^+$ T (T_{EM}) to produce high levels of Granzyme K

987 (GZMK) (**6**), which in turn remodels the tumor microenvironment (TME) fostering EMT (**7**).

988 A $GZMK^{high}$ T_{EM} transcriptional signature effectively stratify non-metastatic early CRC

989 patients and predict poor clinical outcome.

990

991

992 **SUPPLEMENTARY INFORMATIONS**

993 *Availability of supporting data*

994 All data supporting the findings of this study are available from the corresponding authors

995 upon reasonable request.

996 *Authors' contributions*

997 LN and TM contribute equally. Correspondence to Teresa Manzo (teresa.manzo@ieo.it).

998 ST, TM and LN designed. ST, CC, CS, MB, CBNL, GR performed experiments; ST, CC,

999 CS, OC, MB, DC, CS, CBNL, ADM, GB, VL, PP, GR, MS, SC, LN and TM analyzed data;

1000 MR, EL provided critical expertise and resources; WP, SPR, NF and UFR obtained tissues

1001 from patients; LN and TM coordinated the whole study; ST, CC, LN and TM wrote and edited

1002 the manuscript. All the authors discussed and read the manuscript.

1003 *Acknowledgements*

1004 LN and TM dedicate this work to Leonardo and Lara Nezi. We thank Phil Greenberg for

1005 thoughtful discussion. The authors thanks IEO Biobank B4Me, all the nurses, the Molecular

1006 Pathology, Imaging and Genomic Unit at the Department of Experimental Oncology at IEO,

1007 patients abd their families involved in the study.

1008

1009

1010 **BIBLIOGRAPHY**

1011 Aldinucci, D., Borghese, C., and Casagrande, N. (2020). The CCL5/CCR5 Axis in Cancer

1012 Progression. Cancers 2020, Vol. 12, Page 1765 *12*, 1765.

1013 American Cancer Society (2018). Colorectal Cancer Screening Test Use* (%), Adults 50

1014 Years and Older by State, 2018.

1015 Arase, N., Takeuchi, A., Unno, M., Hirano, S., Yokosuka, T., Arase, H., and Saito, T. (2005).

1016 Heterotypic interaction of CRTAM with Necl2 induces cell adhesion on activated NK cells
1017 and CD8+ T cells. Int. Immunol. *17*, 1227–1237.
1018 Ballesteros, I., Rubio-Ponce, A., Genua, M., Lusito, E., Kwok, I., Fernández-Calvo, G.,
1019 Khoyratty, T.E., van Grinsven, E., González-Hernández, S., Nicolás-Ávila, J.Á., et al. (2020).
1020 Co-option of Neutrophil Fates by Tissue Environments. Cell *183*, 1282-1297.e18.
1021 Bankhead, P., Loughrey, M.B., Fernández, J.A., Dombrowski, Y., McArt, D.G., Dunne, P.D.,
1022 McQuaid, S., Gray, R.T., Murray, L.J., Coleman, H.G., et al. (2017). QuPath: Open source
1023 software for digital pathology image analysis. Sci. Reports 2017 71 *7*, 1–7.
1024 Berry, R.S., Xiong, M.J., Greenbaum, A., Mortaji, P., Nofchissey, R.A., Schultz, F., Martinez,
1025 C., Luo, L., Morris, K.T., and Hanson, J.A. (2017). High levels of tumor-associated
1026 neutrophils are associated with improved overall survival in patients with stage II colorectal
1027 cancer. PLoS One *12*.
1028 Binnewies, M., Roberts, E.W., Kersten, K., Chan, V., Fearon, D.F., Merad, M., Coussens,
1029 L.M., Gabrilovich, D.I., Ostrand-Rosenberg, S., Hedrick, C.C., et al. (2018). Understanding
1030 the tumor immune microenvironment (TIME) for effective therapy. Nat. Med. *24*, 541–550.
1031 Bouwman, A.C., van Daalen, K.R., Crnko, S., ten Broeke, T., and Bovenschen, N. (2021).
1032 Intracellular and Extracellular Roles of Granzyme K. Front. Immunol. *12*.
1033 Bronte, V., Brandau, S., Chen, S.-H., Colombo, M.P., Frey, A.B., Greten, T.F., Mandruzzato,
1034 S., Murray, P.J., Ochoa, A., Ostrand-Rosenberg, S., et al. (2016). Recommendations for
1035 myeloid-derived suppressor cell nomenclature and characterization standards. Nat.
1036 Commun. 2016 71 *7*, 1–10.
1037 Buckley, C.D., Ross, E.A., McGettrick, H.M., Osborne, C.E., Haworth, O., Schmutz, C.,
1038 Stone, P.C.W., Salmon, M., Matharu, N.M., Vohra, R.K., et al. (2006). Identification of a
1039 phenotypically and functionally distinct population of long-lived neutrophils in a model of
1040 reverse endothelial migration. J. Leukoc. Biol. *79*, 303–311.
1041 C, M., PC, B., G, B., JC, G.-R., TJ, W., and SM, R. (2003). Chemokines acting via CXCR2

1042 and CXCR4 control the release of neutrophils from the bone marrow and their return
1043 following senescence. Immunity *19*, 583–593.
1044 Carus, A., Ladekarl, M., Hager, H., Pilegaard, H., Nielsen, P.S., and Donskov, F. (2013).
1045 Tumor-associated neutrophils and macrophages in non-small cell lung cancer: No
1046 immediate impact on patient outcome. Lung Cancer *81*, 130–137.
1047 Caruso, R., Sarra, M., Stolfi, C., Rizzo, A., Fina, D., Fantini, M.C., Pallone, F., MacDonald,
1048 T.T., and Monteleone, G. (2009). Interleukin-25 Inhibits Interleukin-12 Production and Th1
1049 Cell-Driven Inflammation in the Gut. Gastroenterology *136*, 2270–2279.
1050 Cerami, E., Gao, J., Dogrusoz, U., Gross, B.E., Sumer, S.O., Aksoy, B.A., Jacobsen, A.,
1051 Byrne, C.J., Heuer, M.L., Larsson, E., et al. (2012). The cBio Cancer Genomics Portal: An
1052 open platform for exploring multidimensional cancer genomics data. Cancer Discov. *2*, 401–
1053 404.
1054 von Chamier, L., Laine, R.F., Jukkala, J., Spahn, C., Krentzel, D., Nehme, E., Lerche, M.,
1055 Hernández-Pérez, S., Mattila, P.K., Karinou, E., et al. (2021). Democratising deep learning
1056 for microscopy with ZeroCostDL4Mic. Nat. Commun. 2021 121 *12*, 1–18.
1057 Chiba, T., Ohtani, H., Mizoi, T., Naito, Y., Sato, E., Nagura, H., Ohuchi, A., Ohuchi, K.,
1058 Shiiba, K., Kurokawa, Y., et al. (2004). Intraepithelial CD8+ T-cell-count becomes a
1059 prognostic factor after a longer follow-up period in human colorectal carcinoma: Possible
1060 association with suppression of micrometastasis. Br. J. Cancer *91*, 1711–1717.
1061 Chiou, S.H., Tseng, D., Reuben, A., Mallajosyula, V., Molina, I.S., Conley, S., Wilhelmy, J.,
1062 McSween, A.M., Yang, X., Nishimiya, D., et al. (2021). Global analysis of shared T cell
1063 specificities in human non-small cell lung cancer enables HLA inference and antigen
1064 discovery. Immunity *54*, 586-602.e8.
1065 Coffelt, S.B., Wellenstein, M.D., and De Visser, K.E. (2016). Neutrophils in cancer: Neutral
1066 no more. Nat. Rev. Cancer *16*, 431–446.
1067 Corbett, T.H., Griswold Jr., D.P., Roberts, B.J., Peckham, J.C., and Schabel Jr., F.M.

1068 (1975). Tumor induction relationships in development of transplantable cancers of the colon
1069 in mice for chemotherapy assays, with a note on carcinogen structure. Cancer Res *35*,
1070 2434–2439.
1071 Corridoni, D., Antanaviciute, A., Gupta, T., Fawkner-Corbett, D., Aulicino, A., Jagielowicz,
1072 M., Parikh, K., Repapi, E., Taylor, S., Ishikawa, D., et al. (2020). Single-cell atlas of colonic
1073 CD8+ T cells in ulcerative colitis. Nat. Med. 2020 269 *26*, 1480–1490.
1074 Cortez, V.S., Cervantes-Barragan, L., Song, C., Gilfillan, S., McDonald, K.G., Tussiwand,
1075 R., Edelson, B.T., Murakami, Y., Murphy, K.M., Newberry, R.D., et al. (2014). CRTAM
1076 controls residency of gut CD4+CD8+ T cells in the steady state and maintenance of gut
1077 CD4+ Th17 during parasitic infection. J. Exp. Med. *211*, 623–633.
1078 Cox, G., Crossley, J., and Xing, Z. (1995). Macrophage engulfment of apoptotic neutrophils
1079 contributes to the resolution of acute pulmonary inflammation in vivo. Am. J. Respir. Cell
1080 Mol. Biol. *12*, 232–237.
1081 Duhen, T., Duhen, R., Montler, R., Moses, J., Moudgil, T., De Miranda, N.F., Goodall, C.P.,
1082 Blair, T.C., Fox, B.A., McDermott, J.E., et al. (2018). Co-expression of CD39 and CD103
1083 identifies tumor-reactive CD8 T cells in human solid tumors. Nat. Commun. *9*.
1084 Eruslanov, E.B., Bhojnagarwala, P.S., Quatromoni, J.G., Stephen, T.L., Ranganathan, A.,
1085 Deshpande, C., Akimova, T., Vachani, A., Litzky, L., Hancock, W.W., et al. (2014). Tumor-
1086 associated neutrophils stimulate T cell responses in early-stage human lung cancer. J. Clin.
1087 Invest. *124*, 5466–5480.
1088 Fergusson, J.R., Hühn, M.H., Swadling, L., Walker, L.J., Kurioka, A., Llibre, A., Bertoletti,
1089 A., Holländer, G., Newell, E.W., Davis, M.M., et al. (2015). CD161intCD8+ T cells: a novel
1090 population of highly functional, memory CD8+ T cells enriched within the gut. Mucosal
1091 Immunol. 2016 92 *9*, 401–413.
1092 Ferrante, A. CD8+ T cells infiltrated within cancer cell nests as a prognostic factor in human
1093 colorectal cancer.

1094 Filippo, K. De, and Rankin, S.M. (2018). CXCR4, the master regulator of neutrophil
1095 trafficking in homeostasis and disease. Eur. J. Clin. Invest. *48*.
1096 Fort, M.M., Cheung, J., Yen, D., Li, J., Zurawski, S.M., Lo, S., Menon, S., Clifford, T., Hunte,
1097 B., Lesley, R., et al. (2001). IL-25 Induces IL-4, IL-5, and IL-13 and Th2-Associated
1098 Pathologies In Vivo. Immunity *15*, 985–995.
1099 Fountzilas, E., Kotoula, V., Tikas, I., Manousou, K., Papadopoulou, K., Poulios, C.,
1100 Karavasilis, V., Efstratiou, I., Pectasides, D., Papaparaskeva, K., et al. (2018). Prognostic
1101 significance of tumor genotypes and CD8+ infiltrates in stage I-III colorectal cancer.
1102 Oncotarget *9*, 35623–35638.
1103 Fridlender, Z.G., Sun, J., Kim, S., Kapoor, V., Cheng, G., Ling, L., Worthen, G.S., and
1104 Albelda, S.M. (2009). Polarization of Tumor-Associated Neutrophil Phenotype by TGF-β:
1105 "N1" versus "N2" TAN. Cancer Cell *16*, 183–194.
1106 Galdiero, M.R., Varricchi, G., Loffredo, S., Mantovani, A., and Marone, G. (2018). Roles of
1107 neutrophils in cancer growth and progression. J. Leukoc. Biol. *103*, 457–464.
1108 Galibert, L., Diemer, G.S., Liu, Z., Johnson, R.S., Smith, J.L., Walzer, T., Comeau, M.R.,
1109 Rauch, C.T., Wolfson, M.F., Sorensen, R.A., et al. (2005). Nectin-like Protein 2 Defines a
1110 Subset of T-cell Zone Dendritic Cells and Is a Ligand for Class-I-restricted T-cell-associated
1111 Molecule * ♦. J. Biol. Chem. *280*, 21955–21964.
1112 Galon, J., Mlecnik, B., Bindea, G., Angeli, H., Lagorce, C., Marincola, F., Fox, B., and Pagès,
1113 F. (2014). Towards the introduction of the "Immunoscore" in the classification of malignant
1114 tumours. J. Pathol. *232*, 199–209.
1115 Gentles, A.J., Newman, A.M., Liu, C.L., Bratman, S. V., Feng, W., Kim, D., Nair, V.S., Xu,
1116 Y., Khuong, A., Hoang, C.D., et al. (2015). The prognostic landscape of genes and infiltrating
1117 immune cells across human cancers. Nat. Med. *21*, 938–945.
1118 Gerlini, G., Tun-Kyi, A., Dudli, C., Burg, G., Pimpinelli, N., and Nestle, F.O. (2004).
1119 Metastatic Melanoma Secreted IL-10 Down-Regulates CD1 Molecules on Dendritic Cells in

1120 Metastatic Tumor Lesions. Am. J. Pathol. *165*, 1853.
1121 Gholamin, M., Moaven, O., Memar, B., Farshchian, M., Naseh, H., Malekzadeh, R.,
1122 Sotoudeh, M., Rajabi-Mashhadi, M.T., Forghani, M.N., Farrokhi, F., et al. (2009).
1123 Overexpression and interactions of interleukin-10, transforming growth factor β, and
1124 vascular endothelial growth factor in esophageal squamous cell carcinoma. World J. Surg.
1125 *33*, 1439–1445.
1126 Governa, V., Trella, E., Mele, V., Tornillo, L., Amicarella, F., Cremonesi, E., Muraro, M.G.,
1127 Xu, H., Droeser, R., Däster, S.R., et al. (2017). The Interplay Between Neutrophils and
1128 CD8(+) T Cells Improves Survival in Human Colorectal Cancer. Clin Cancer Res *23*, 3847–
1129 3858.
1130 Grigg, J.M., Silverman, M., Savill, J.S., Sarraf, C., and Haslett, C. (1991). Neutrophil
1131 apoptosis and clearance from neonatal lungs. Lancet *338*, 720–722.
1132 Guo, X., Zhang, Y., Zheng, L., Zheng, C., Song, J., Zhang, Q., Kang, B., Liu, Z., Jin, L.,
1133 Xing, R., et al. (2018). Global characterization of T cells in non-small-cell lung cancer by
1134 single-cell sequencing. Nat. Med. *24*, 978–985.
1135 Gustafson, M.P., Lin, Y., Maas, M.L., Keulen, V.P. Van, Johnston, P.B., Peikert, T.,
1136 Gastineau, D.A., and Dietz, A.B. (2015). A Method for Identification and Analysis of Non-
1137 Overlapping Myeloid Immunophenotypes in Humans. PLoS One *10*, e0121546.
1138 Hafemeister, C., and Satija, R. (2019). Normalization and variance stabilization of single-
1139 cell RNA-seq data using regularized negative binomial regression. Genome Biol. 2019 201
1140 *20*, 1–15.
1141 Holmes, G.R., Anderson, S.R., Dixon, G., Robertson, A.L., Reyes-Aldasoro, C.C., Billings,
1142 S.A., Renshaw, S.A., and Kadirkamanathan, V. (2012). Repelled from the wound, or
1143 randomly dispersed? Reverse migration behaviour of neutrophils characterized by dynamic
1144 modelling. J. R. Soc. Interface *9*, 3229–3239.
1145 Hornburg, M., Desbois, M., Lu, S., Guan, Y., Lo, A.A., Kaufman, S., Elrod, A., Lotstein, A.,

1146 DesRochers, T.M., Munoz-Rodriguez, J.L., et al. (2021). Single-cell dissection of cellular
1147 components and interactions shaping the tumor immune phenotypes in ovarian cancer.
1148 Cancer Cell *39*, 928-944.e6.
1149 Htwe, S.S., Wake, H., Liu, K., Teshigawara, K., Stonestreet, B.S., Lim, Y.P., and Nishibori,
1150 M. (2018). Inter-a inhibitor proteins maintain neutrophils in a resting state by regulating
1151 shape and reducing ROS production. Blood Adv. *2*, 1923–1934.
1152 Ilie, M., Hofman, V., Long-Mira, E., Selva, E., Vignaud, J.-M., Padovani, B., Mouroux, J.,
1153 Marquette, C.-H., and Hofman, P. (2014). “Sentinel” Circulating Tumor Cells Allow Early
1154 Diagnosis of Lung Cancer in Patients with Chronic Obstructive Pulmonary Disease. PLoS
1155 One *9*, 111597.
1156 Impellizzieri, D., Ridder, F., Raeber, M.E., Egholm, C., Woytschak, J., Kolios, A.G.A., Legler,
1157 D.F., and Boyman, O. (2019). IL-4 receptor engagement in human neutrophils impairs their
1158 migration and extracellular trap formation. J. Allergy Clin. Immunol. *144*, 267-279.e4.
1159 Isles, H.M., Herman, K.D., Robertson, A.L., Loynes, C.A., Prince, L.R., Elks, P.M., and
1160 Renshaw, S.A. (2019). The CXCL12/CXCR4 Signaling Axis Retains Neutrophils at
1161 Inflammatory Sites in Zebrafish. Front. Immunol. *0*, 1784.
1162 Jaillon, S., Ponzetta, A., Di Mitri, D., Santoni, A., Bonecchi, R., and Mantovani, A. (2020a).
1163 Neutrophil diversity and plasticity in tumour progression and therapy. Nat. Rev. Cancer *20*,
1164 485–503.
1165 Jaillon, S., Ponzetta, A., Di Mitri, D., Santoni, A., Bonecchi, R., and Mantovani, A. (2020b).
1166 Neutrophil diversity and plasticity in tumour progression and therapy. Nat Rev Cancer *20*,
1167 485–503.
1168 Joeckel, L.T., and Bird, P.I. (2014). Are all granzymes cytotoxic in vivo? Biol. Chem. *395*,
1169 181–202.
1170 Joeckel, L.T., Wallich, R., Martin, P., Sanchez-Martinez, D., Weber, F.C., Martin, S.F.,
1171 Borner, C., Pardo, J., Froelich, C., and Simon, M.M. (2011). Mouse granzyme K has pro-

1172 inflammatory potential. Cell Death Differ. *18*, 1112–1119.
1173 Joshita, S., Nakazawa, K., Sugiyama, Y., Kamijo, A., Matsubayashi, K., Miyabayashi, H.,
1174 Furuta, K., Kitano, K., and Kawa, S. (2009). Granulocyte-colony stimulating factor-producing
1175 pancreatic adenosquamous carcinoma showing aggressive clinical course. Intern. Med. *48*,
1176 687–691.
1177 Koch, M., Beckhove, P., Op Den Winkel, J., Autenrieth, D., Wagner, P., Nummer, D.,
1178 Specht, S., Antolovic, D., Galindo, L., Schmitz-Winnenthal, F.H., et al. (2006). Tumor
1179 infiltrating T lymphocytes in colorectal cancer: Tumor-selective activation and cytotoxic
1180 activity in situ. Ann. Surg. *244*, 986–992.
1181 Kyo, S., Kanaya, T., Takakura, M., and Inoue, M. (2000). A case of cervical cancer with
1182 aggressive tumor growth: Possible autocrine growth stimulation by G-CSF and Il-6.
1183 Gynecol. Oncol. *78*, 383–387.
1184 Lavin, Y., Kobayashi, S., Leader, A., Amir, E. ad D., Elefant, N., Bigenwald, C., Remark, R.,
1185 Sweeney, R., Becker, C.D., Levine, J.H., et al. (2017). Innate Immune Landscape in Early
1186 Lung Adenocarcinoma by Paired Single-Cell Analyses. Cell *169*, 750-765.e17.
1187 Levine, J.H., Simonds, E.F., Bendall, S.C., Davis, K.L., Amir, E.A.D., Tadmor, M.D., Litvin,
1188 O., Fienberg, H.G., Jager, A., Zunder, E.R., et al. (2015). Data-Driven Phenotypic Dissection
1189 of AML Reveals Progenitor-like Cells that Correlate with Prognosis. Cell *162*, 184–197.
1190 Li, H., van der Leun, A.M., Yofe, I., Lubling, Y., Gelbard-Solodkin, D., van Akkooi, A.C.J.,
1191 van den Braber, M., Rozeman, E.A., Haanen, J.B.A.G., Blank, C.U., et al. (2019).
1192 Dysfunctional CD8 T Cells Form a Proliferative, Dynamically Regulated Compartment within
1193 Human Melanoma. Cell *176*, 775-789.e18.
1194 Li, P., Lu, M., Shi, J., Gong, Z., Hua, L., Li, Q., Lim, B., Zhang, X.H.F., Chen, X., Li, S., et al.
1195 (2020). Lung mesenchymal cells elicit lipid storage in neutrophils that fuel breast cancer
1196 lung metastasis. Nat. Immunol. *21*, 1444–1455.
1197 Li, Z., Zhao, R., Cui, Y., Zhou, Y., and Wu, X. (2018). The dynamic change of neutrophil to

1198 lymphocyte ratio can predict clinical outcome in stage I-III colon cancer. Sci. Reports 2018
1199 81 *8*, 1–8.
1200 M, S., Y, M., S, R., LG, P., Y, S., D, C., and DJ, G. (2016). Extracellular granzyme K
1201 mediates endothelial activation through the cleavage of protease-activated receptor-1.
1202 FEBS J. *283*, 1734–1747.
1203 MA, H., N, K., and H, B. (2005). Molecular requirements for epithelial-mesenchymal
1204 transition during tumor progression. Curr. Opin. Cell Biol. *17*, 548–558.
1205 Mantovani, A., Cassatella, M.A., Costantini, C., and Jaillon, S. (2011). Neutrophils in the
1206 activation and regulation of innate and adaptive immunity. Nat. Rev. Immunol. *11*, 519–531.
1207 Marini, O., Costa, S., Bevilacqua, D., Calzetti, F., Tamassia, N., Spina, C., De Sabata, D.,
1208 Tinazzi, E., Lunardi, C., Scupoli, M.T., et al. (2017). Mature CD10+ and immature CD10-
1209 neutrophils present in G-CSF-treated donors display opposite effects on T cells. Blood *129*,
1210 1343–1356.
1211 McLane, L.M., Abdel-Hakeem, M.S., and Wherry, E.J. (2019). CD8 T Cell Exhaustion During
1212 Chronic Viral Infection and Cancer. Annu. Rev. Immunol. *37*, 457–495.
1213 Mogilenko, D.A., Shpynov, O., Andhey, P.S., Arthur, L., Swain, A., Esaulova, E., Brioschi,
1214 S., Shchukina, I., Kerndl, M., Bambouskova, M., et al. (2021). Comprehensive Profiling of
1215 an Aging Immune System Reveals Clonal GZMK+ CD8+ T Cells as Conserved Hallmark of
1216 Inflammaging. Immunity *54*, 99-115.e12.
1217 Moore, K.W., De Waal Malefyt, R., Coffman, R.L., and O'Garra, A. (2001). Interleukin-10
1218 and the interleukin-10 receptor. Annu. Rev. Immunol. *19*, 683–765.
1219 Naito, Y., Saito, K., Shiiba, K., Ohuchi, A., Saigenji, K., Nagura, H., and Ohtani, H. (1998).
1220 CD8+ T Cells Infiltrated within Cancer Cell Nests as a Prognostic Factor in Human
1221 Colorectal Cancer. Cancer Res. *58*.
1222 Nathan, C., and Ding, A. (2010). Nonresolving Inflammation. Cell *140*, 871–882.
1223 Ogino, S., Nosho, K., Irahara, N., Meyerhardt, J.A., Baba, Y., Shima, K., Glickman, J.N.,

1224 Ferrone, C.R., Mino-Kenudson, M., Tanaka, N., et al. (2009). Lymphocytic reaction to
1225 colorectal cancer is associated with longer survival, independent of lymph node count,
1226 microsatellite instability, and CpG island methylator phenotype. Clin. Cancer Res. *15*, 6412–
1227 6420.
1228 Owyang, A.M., Zaph, C., Wilson, E.H., Guild, K.J., McClanahan, T., Miller, H.R.P., Cua,
1229 D.J., Goldschmidt, M., Hunter, C.A., Kastelein, R.A., et al. (2006). Interleukin 25 regulates
1230 type 2 cytokine-dependent immunity and limits chronic inflammation in the gastrointestinal
1231 tract. J. Exp. Med. *203*, 843–849.
1232 Pagès, F., Kirilovsky, A., and ...Galon, J. (2009a). In situ cytotoxic and memory T cells
1233 predict outcome in patients with early-stage colorectal cancer. J. Clin. Oncol. *27*, 5944–
1234 5951.
1235 Pagès, F., Berger, A., Camus, M., Sanchez-Cabo, F., Costes, A., Molidor, R., Mlecnik, B.,
1236 Kirilovsky, A., Nilsson, M., Damotte, D., et al. (2009b). Effector Memory T Cells, Early
1237 Metastasis, and Survival in Colorectal Cancer. Http://Dx.Doi.Org/10.1056/NEJMoa051424
1238 *353*, 2654–2666.
1239 Pagès, F., Kirilovsky, A., Mlecnik, B., Asslaber, M., Berger, A., Fridman, W., and Galon, J.
1240 (2009c). In situ cytotoxic and memory T cells predict outcome in patients with early-stage
1241 colorectal cancer. J. Clin. Oncol. *27*, 5944–5951.
1242 Peng, Z., Liu, C., Victor, A.R., Cao, D.Y., Veiras, L.C., Bernstein, E.A., Khan, Z., Giani, J.F.,
1243 Cui, X., Bernstein, K.E., et al. (2021a). Tumors exploit CXCR4hiCD62Llo aged neutrophils
1244 to facilitate metastatic spread. Oncoimmunology *10*.
1245 Peng, Z., Liu, C., Victor, A.R., Cao, D.-Y., Veiras, L.C., Bernstein, E.A., Khan, Z., Giani, J.F.,
1246 Cui, X., Bernstein, K.E., et al. (2021b). Tumors exploit CXCR4hiCD62Llo aged neutrophils
1247 to facilitate metastatic spread. Https://Doi.Org/10.1080/2162402X.2020.1870811 *10*.
1248 Pillay, J., Tak, T., Kamp, V.M., and Koenderman, L. (2013). Immune suppression by
1249 neutrophils and granulocytic myeloid-derived suppressor cells: Similarities and differences.

1250 Cell. Mol. Life Sci. *70*, 3813–3827.

1251 Powell, D., Tauzin, S., Hind, L.E., Deng, Q., Beebe, D.J., and Huttenlocher, A. (2017).
1252 Chemokine Signaling and the Regulation of Bidirectional Leukocyte Migration in Interstitial
1253 Tissues. Cell Rep. *19*, 1572–1585.

1254 Prall, F., Dührkop, T., Weirich, V., Ostwald, C., Lenz, P., Nizze, H., and Barten, M. (2004).
1255 Prognostic role of CD8+ tumor-infiltrating lymphocytes in stage III colorectal cancer with and
1256 without microsatellite instability. Hum. Pathol. *35*, 808–816.

1257 Rao, H.L., Chen, J.W., Li, M., Xiao, Y.B., Fu, J., Zeng, Y.X., Cai, M.Y., and Xie, D. (2012).
1258 Increased intratumoral neutrophil in colorectal carcinomas correlates closely with malignant
1259 phenotype and predicts patients' adverse prognosis. PLoS One *7*.

1260 Robertson, A.L., Holmes, G.R., Bojarczuk, A.N., Burgon, J., Loynes, C.A., Chimen, M.,
1261 Sawtell, A.K., Hamza, B., Willson, J., Walmsley, S.R., et al. (2014). A zebrafish compound
1262 screen reveals modulation of neutrophil reverse migration as an anti-inflammatory
1263 mechanism. Sci. Transl. Med. *6*.

1264 Rock, K.L., Latz, E., Ontiveros, F., and Kono, H. (2010). The sterile inflammatory response.
1265 Annu. Rev. Immunol. *28*, 321–342.

1266 Romero, P., Zippelius, A., Kurth, I., Pittet, M.J., Touvrey, C., Iancu, E.M., Corthesy, P.,
1267 Devevre, E., Speiser, D.E., and Rufer, N. (2007). Four Functionally Distinct Populations of
1268 Human Effector-Memory CD8 + T Lymphocytes. J. Immunol. *178*, 4112–4119.

1269 Rooney, M.S., Shukla, S.A., Wu, C.J., Getz, G., and Hacohen, N. (2015). Molecular and
1270 genetic properties of tumors associated with local immune cytolytic activity. Cell *160*, 48–
1271 61.

1272 Salmon, H., Idoyaga, J., Rahman, A., Leboeuf, M., Remark, R., Jordan, S., Casanova-
1273 Acebes, M., Khudoynazarova, M., Agudo, J., Tung, N., et al. (2016). Expansion and
1274 Activation of CD103+ Dendritic Cell Progenitors at the Tumor Site Enhances Tumor
1275 Responses to Therapeutic PD-L1 and BRAF Inhibition. Immunity *44*, 924–938.

1276 Sangaletti, S., Tripodo, C., Vitali, C., Portararo, P., Guarnotta, C., Casalini, P., Cappetti, B.,
1277 Miotti, S., Pinciroli, P., Fuligni, F., et al. (2014a). Defective Stromal Remodeling and
1278 Neutrophil Extracellular Traps in Lymphoid Tissues Favor the Transition from Autoimmunity
1279 to Lymphoma. Cancer Discov. *4*, 110–129.
1280 Sangaletti, S., Tripodo, C., Vitali, C., Portararo, P., Guarnotta, C., Casalini, P., Cappetti, B.,
1281 Miotti, S., Pinciroli, P., Fuligni, F., et al. (2014b). Defective stromal remodeling and neutrophil
1282 extracellular traps in lymphoid tissues favor the transition from autoimmunity to lymphoma.
1283 Cancer Discov *4*, 110–129.
1284 Schall, T.J., Bacon, K., Toy, K.J., and Goeddel, D. V. (1990). Selective attraction of
1285 monocytes and T lymphocytes of the memory phenotype by cytokine RANTES. Nature *347*,
1286 669–671.
1287 Scheper, W., Kelderman, S., Fanchi, L.F., Linnemann, C., Bendle, G., de Rooij, M.A.J., Hirt,
1288 C., Mezzadra, R., Slagter, M., Dijkstra, K., et al. (2019). Low and variable tumor reactivity of
1289 the intratumoral TCR repertoire in human cancers. Nat. Med. *25*, 89–94.
1290 Schindelin, J., Arganda-Carreras, I., Frise, E., Kaynig, V., Longair, M., Pietzsch, T.,
1291 Preibisch, S., Rueden, C., Saalfeld, S., Schmid, B., et al. (2012). Fiji: an open-source
1292 platform for biological-image analysis. Nat. Methods 2012 97 *9*, 676–682.
1293 Schmidt, U., Weigert, M., Broaddus, C., and Myers, G. (2018). Cell detection with star-
1294 convex polygons. In Lecture Notes in Computer Science (Including Subseries Lecture Notes
1295 in Artificial Intelligence and Lecture Notes in Bioinformatics), (Springer, Cham), pp. 265–
1296 273.
1297 Senra, L., Mylonas, A., Kavanagh, R.D., Fallon, P.G., Conrad, C., Borowczyk-Michalowska,
1298 J., Wrobel, L.J., Kaya, G., Yawalkar, N., Boehncke, W.H., et al. (2019). IL-17E (IL-25)
1299 Enhances Innate Immune Responses during Skin Inflammation. J. Invest. Dermatol. *139*,
1300 1732-1742.e17.
1301 Seo, W., Shimizu, K., Kojo, S., Okeke, A., Kohwi-Shigematsu, T., Fujii, S., and Taniuchi, I.

1302 (2020). Runx-mediated regulation of CCL5 via antagonizing two enhancers influences
1303 immune cell function and anti-tumor immunity. Nat. Commun. 2020 111 *11*, 1–16.
1304 Shaul, M.E., and Fridlender, Z.G. (2019). Tumour-associated neutrophils in patients with
1305 cancer. Nat. Rev. Clin. Oncol. 2019 1610 *16*, 601–620.
1306 Shelley, M., Ross, C., and Nizet, V. (2018). The Ontogeny of a Neutrophil: Mechanisms of
1307 Granulopoiesis and Homeostasis. Microbiol. Mol. Biol. Rev. *82*.
1308 Silvestre-Roig, C., Fridlender, Z.G., Glogauer, M., and Scapini, P. (2019). Neutrophil
1309 Diversity in Health and Disease. Trends Immunol. *40*, 565–583.
1310 Simoni, Y., Becht, E., Fehlings, M., Loh, C.Y., Koo, S.L., Teng, K.W.W., Yeong, J.P.S.,
1311 Nahar, R., Zhang, T., Kared, H., et al. (2018). Bystander CD8+ T cells are abundant and
1312 phenotypically distinct in human tumour infiltrates. Nature *557*, 575–579.
1313 Singhal, S., Bhojnagarwala, P.S., O'Brien, S., Moon, E.K., Garfall, A.L., Rao, A.S.,
1314 Quatromoni, J.G., Stephen, T.L., Litzky, L., Deshpande, C., et al. (2016). Origin and Role of
1315 a Subset of Tumor-Associated Neutrophils with Antigen-Presenting Cell Features in Early-
1316 Stage Human Lung Cancer. Cancer Cell *30*, 120–135.
1317 Stuart, T., Butler, A., Hoffman, P., Hafemeister, C., Papalexi, E., Mauck, W.M., Hao, Y.,
1318 Stoeckius, M., Smibert, P., and Satija, R. (2019). Comprehensive Integration of Single-Cell
1319 Data. Cell *177*, 1888-1902.e21.
1320 Sun, H., Zhou, Y., Fei, L., Chen, H., and Guo, G. (2019). scMCA: A tool to define mouse cell
1321 types based on single-cell digital expression. In Methods in Molecular Biology, (Methods
1322 Mol Biol), pp. 91–96.
1323 Swanson, B.J., Murakami, M., Mitchell, T.C., Kappler, J., and Marrack, P. (2002). RANTES
1324 production by memory phenotype T cells is controlled by a posttranscriptional, TCR-
1325 dependent process. Immunity *17*, 605–615.
1326 Thome, J.J.C., and Farber, D.L. (2015). Emerging concepts in tissue-resident T cells:
1327 Lessons from humans. Trends Immunol. *36*, 428–435.

1328 Walzer, T., Marçais, A., Saltel, F., Bella, C., Jurdic, P., and Marvel, J. (2003). Cutting Edge:
1329 Immediate RANTES Secretion by Resting Memory CD8 T Cells Following Antigenic
1330 Stimulation. J. Immunol. *170*, 1615–1619.
1331 Wang, A.J., Smith, A., Li, Y., Urban, J.F., Ramalingam, T.R., Wynn, T.A., Lu, N., Shea-
1332 Donohue, T., Yang, Z., and Zhao, A. (2014). Genetic deletion of IL-25 (IL-17E) confers
1333 resistance to dextran sulfate sodium-induced colitis in mice. Cell Biosci. *4*.
1334 Wang, J., Hossain, M., Thanabalasuriar, A., Gunzer, M., Meininger, C., and Kubes, P.
1335 (2017). Visualizing the function and fate of neutrophils in sterile injury and repair. Science
1336 (80-.). *358*, 111–116.
1337 Weinstein, J.N., Collisson, E.A., Mills, G.B., Shaw, K.R.M., Ozenberger, B.A., Ellrott, K.,
1338 Sander, C., Stuart, J.M., Chang, K., Creighton, C.J., et al. (2013). The cancer genome atlas
1339 pan-cancer analysis project. Nat. Genet. *45*, 1113–1120.
1340 Wensink, A.C., Kemp, V., Fermie, J., Laorden, M.I.G., Van Der Poll, T., Hack, C.E., and
1341 Bovenschen, N. (2014). Granzyme K synergistically potentiates LPS-induced cytokine
1342 responses in human monocytes. Proc. Natl. Acad. Sci. U. S. A. *111*, 5974–5979.
1343 Wensink, A.C., Hack, C.E., and Bovenschen, N. (2015). Granzymes Regulate
1344 Proinflammatory Cytokine Responses. J. Immunol. *194*, 491–497.
1345 Woodfin, A., Voisin, M.B., Beyrau, M., Colom, B., Caille, D., Diapouli, F.M., Nash, G.B.,
1346 Chavakis, T., Albelda, S.M., Rainger, G.E., et al. (2011). The junctional adhesion molecule
1347 JAM-C regulates polarized transendothelial migration of neutrophils in vivo. Nat. Immunol.
1348 *12*, 761–769.
1349 Wu, P., Wu, D., Ni, C., Ye, J., Chen, W., Hu, G., Wang, Z., Wang, C., Zhang, Z., Xia, W., et
1350 al. (2014). γδT17 cells promote the accumulation and expansion of myeloid-derived
1351 suppressor cells in human colorectal cancer. Immunity *40*, 785–800.
1352 Zeisberg, M., and Neilson, E.G. (2009). Biomarkers for epithelial-mesenchymal transitions.
1353 J. Clin. Invest. *119*, 1429–1437.

1354 Zhang, L., Yu, X., Zheng, L., Zhang, Y., Li, Y., Fang, Q., Gao, R., Kang, B., Zhang, Q.,
1355 Huang, J.Y., et al. (2018). Lineage tracking reveals dynamic relationships of T cells in
1356 colorectal cancer. Nature *564*, 268–272.
1357 Zlobec, I., Karamitopoulou, E., Terracciano, L., Piscuoglio, S., Iezzi, G., Muraro, M.G.,
1358 Spagnoli, G., Baker, K., Tzankov, A., and Lugli, A. (2010). TIA-1 Cytotoxic Granule-
1359 Associated RNA Binding Protein Improves the Prognostic Performance of CD8 in Mismatch
1360 Repair-Proficient Colorectal Cancer. PLoS One *5*, e14282.
1361

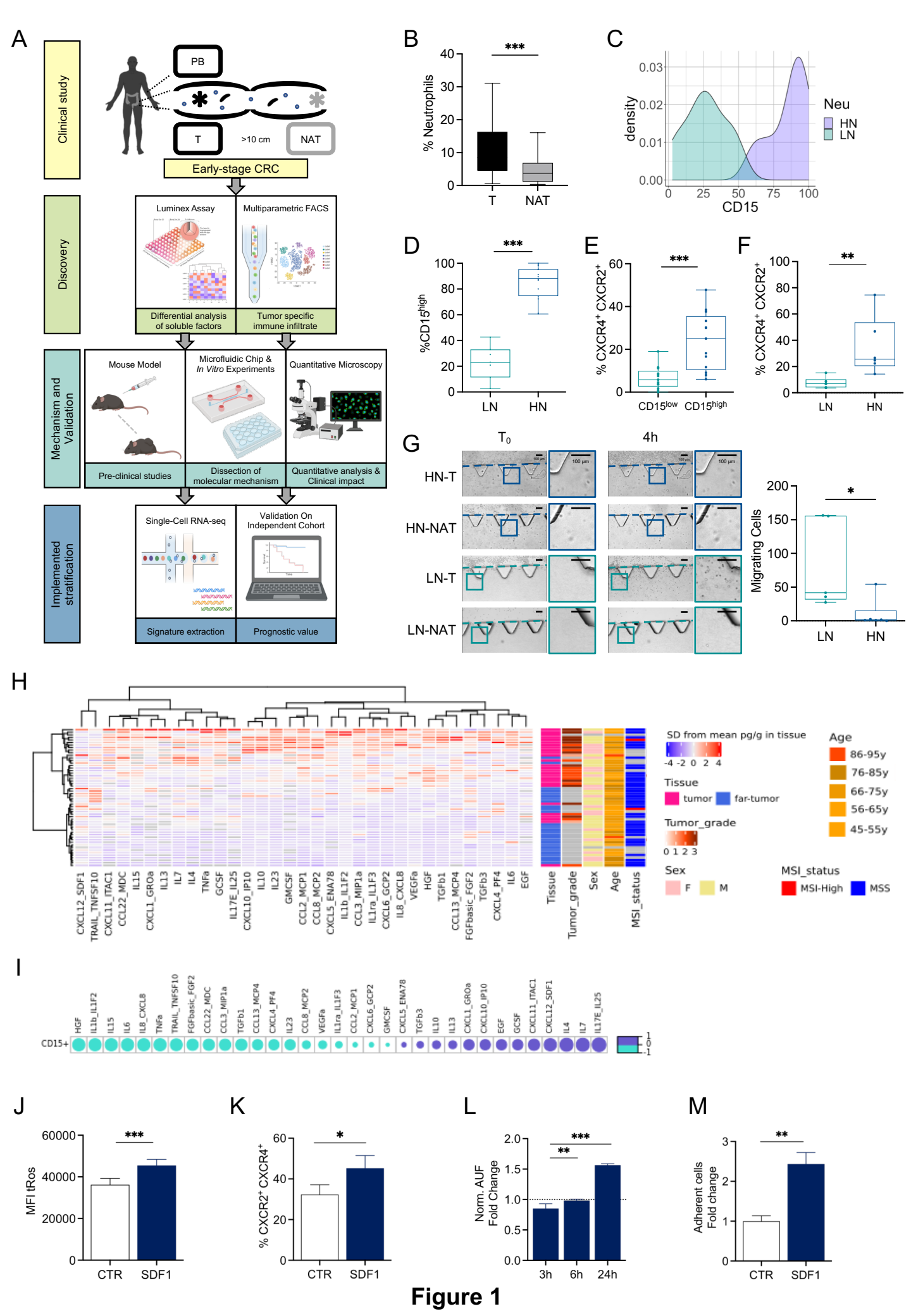
A
Clinical study
PB
T
>10 cm
NAT
Early-stage CRC
Discovery
Luminex Assay
Multiparametric FACS
Differential analysis of soluble factors
Tumor specific immune infiltrate
Mechanism and Validation
Mouse Model
Microfluidic Chip & In Vitro Experiments
Quantitative Microscopy
Pre-clinical studies
Dissection of molecular mechanism
Quantitative analysis & Clinical impact
Implemented stratification
Single-Cell RNA-seq
Validation On Independent Cohort
Signature extraction
Prognostic value
B
% Neutrophils
T
NAT
C
density
CD15
Neu
HN
LN
D
%CD15high
LN
HN
E
% CXCR4+ CXCR2+
CD15low
CD15high
F
% CXCR4+ CXCR2+
LN
HN
G
T0
4h
HN-T
HN-NAT
LN-T
LN-NAT
Migrating Cells
LN
HN
H
SD from mean pg/g in tissue
Tissue
tumor
far-tumor
Tumor_grade
Age
86-95y
76-85y
66-75y
56-65y
45-55y
Sex
F
M
MSI_status
MSI-High
MSS
CXCL12_SDF1
TRAIL_TNFSF10
CXCL11_ITAC1
CCL22_MDC
IL15
CXCL1_GROa
IL13
IL7
IL4
TNFa
GCSF
IL17E_IL25
CXCL10_IP10
IL10
IL23
GMCSF
CCL2_MCP1
CCL8_MCP2
CXCL5_ENA78
IL1b_IL1F2
CCL3_MIP1a
IL1ra_IL1F3
CXCL6_GCP2
IL8_CXCL8
VEGFa
HGF
TGFb1
CCL13_MCP4
FGFbasic_FGF2
TGFb3
CXCL4_PF4
IL6
EGF
Tissue
Tumor_grade
Sex
Age
MSI_status
I
CD15+
HGF
IL1b_IL1F2
IL15
IL6
IL8_CXCL8
TNFa
TRAIL_TNFSF10
FGFbasic_FGF2
CCL22_MDC
CCL3_MIP1a
TGFb1
CCL13_MCP4
CXCL4_PF4
IL23
CCL8_MCP2
VEGFa
IL1ra_IL1F3
CCL2_MCP1
CXCL6_GCP2
GMCSF
CXCL5_ENA78
TGFb3
IL10
IL13
CXCL1_GROa
CXCL10_IP10
EGF
GCSF
CXCL11_ITAC1
CXCL12_SDF1
IL4
IL7
IL17E_IL25
J
MFI tRos
CTR
SDF1
K
% CXCR2+ CXCR4+
CTR
SDF1
L
Norm. AUF Fold Change
3h
6h
24h
M
Adherent cells Fold change
CTR
SDF1

Figure 1

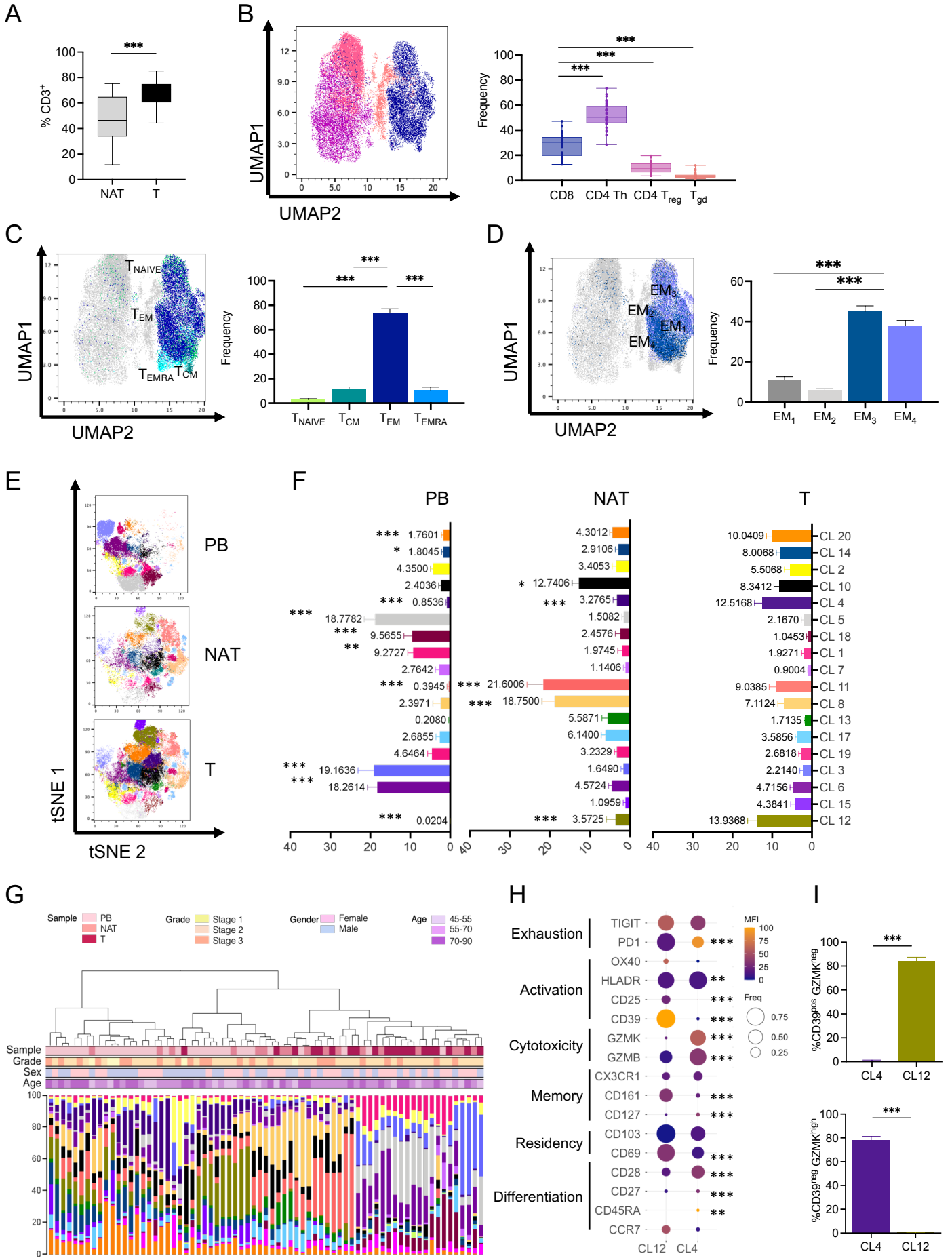
A
% CD3+
NAT
T
B
UMAP1
UMAP2
Frequency
CD8
CD4 Th
CD4 Treg
Tgd
C
TNAIVE
TEM
TEMRA
TCM
D
EM1
EM2
EM3
EM4
E
PB
NAT
T
tSNE 1
tSNE 2
F
PB
NAT
T
CL 20
CL 14
CL 2
CL 10
CL 4
CL 5
CL 18
CL 1
CL 7
CL 11
CL 8
CL 13
CL 17
CL 19
CL 3
CL 6
CL 15
CL 12
G
Sample
PB
NAT
T
Grade
Stage 1
Stage 2
Stage 3
Gender
Female
Male
Age
45-55
55-70
70-90
Sex
H
Exhaustion
TIGIT
PD1
Activation
OX40
HLADR
CD25
CD39
Cytotoxicity
GZMK
GZMB
Memory
CX3CR1
CD161
CD127
Residency
CD103
CD69
Differentiation
CD28
CD27
CD45RA
CCR7
CL12
CL4
MFI
Freq
I
%CD39pos GZMKneg
%CD39neg GZMKhigh
CL4
CL12

Figure 2

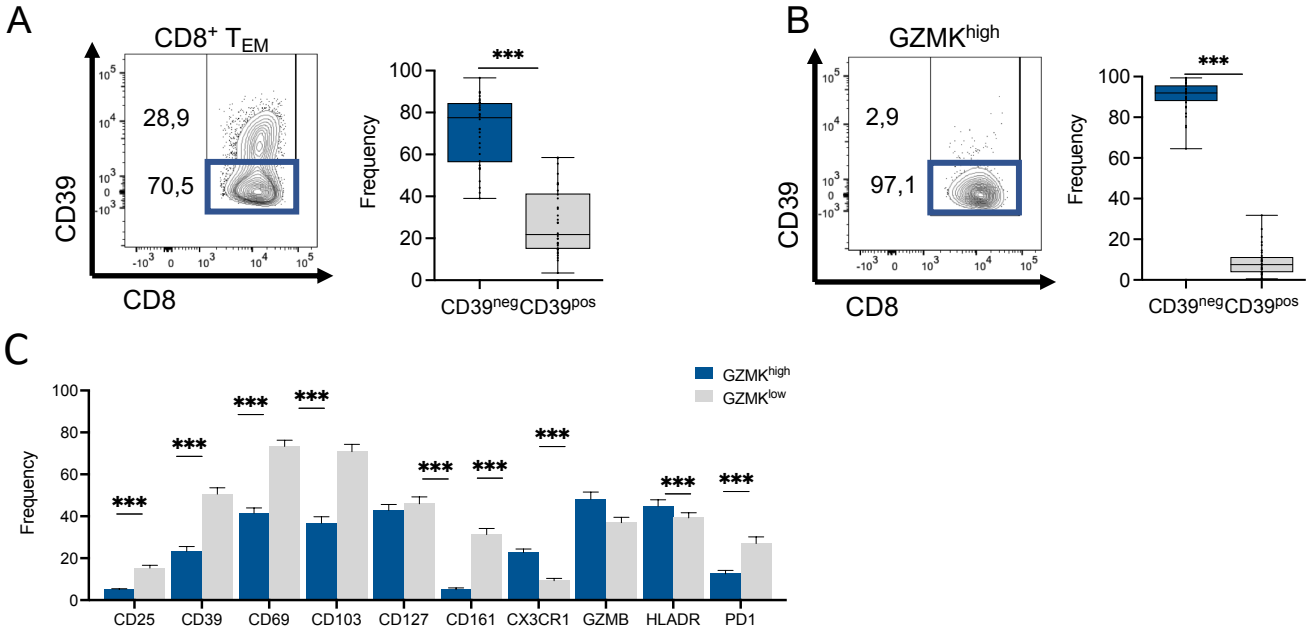
A
CD8+ TEM
28,9
70,5
CD39
CD8
Frequency
***
CD39negCD39pos
B
GZMKhigh
2,9
97,1
CD39
CD8
Frequency
***
CD39negCD39pos
C
GZMKhigh
GZMKlow
Frequency
CD25
CD39
CD69
CD103
CD127
CD161
CX3CR1
GZMB
HLADR
PD1

Figure 3

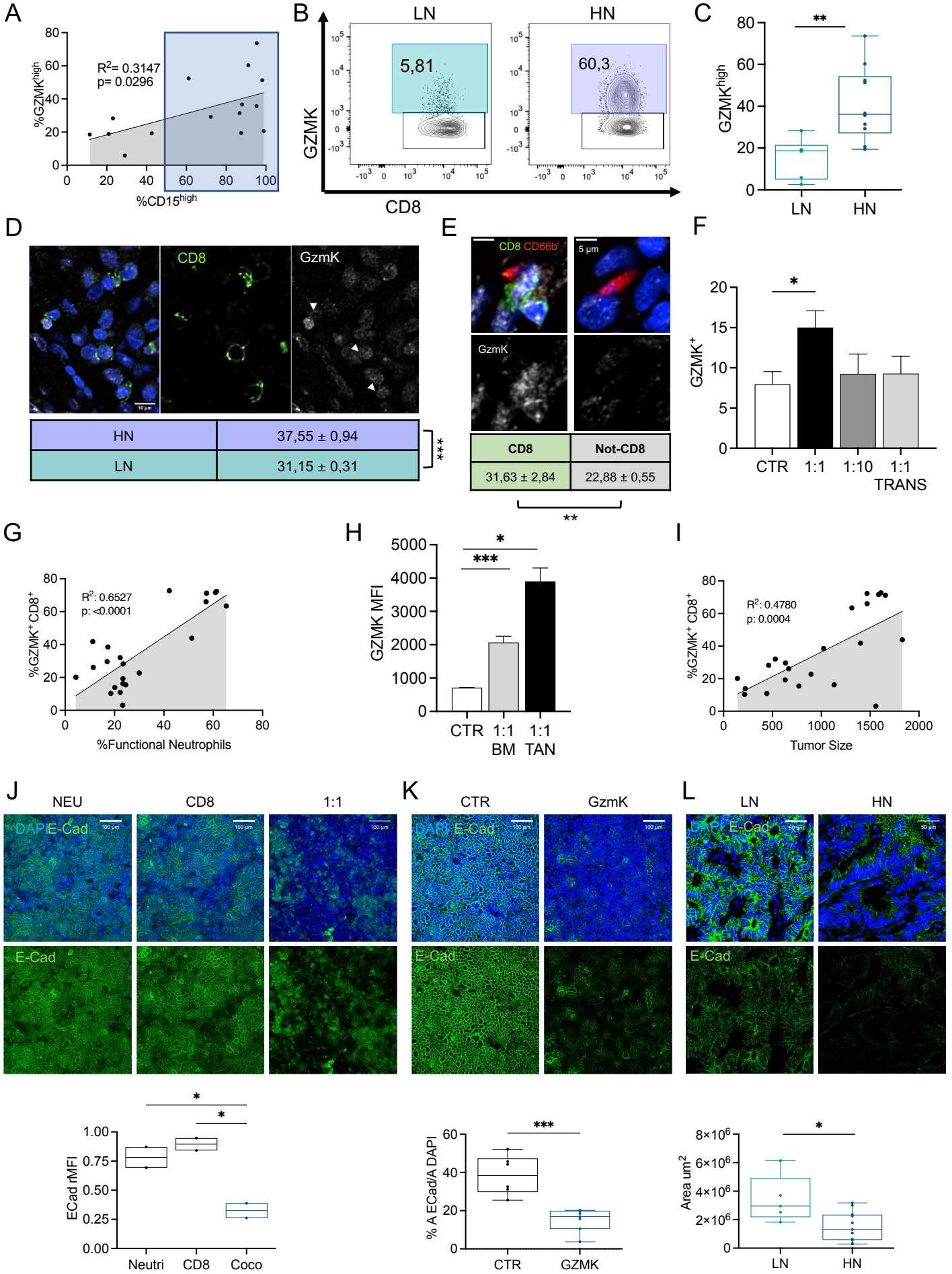
A
R2= 0.3147
p= 0.0296
%GZMKhigh
%CD15high
B
LN
HN
5,81
60,3
GZMK
CD8
C
GZMKhigh
LN
HN
D
CD8
GzmK
HN 37,55 ± 0,94
LN 31,15 ± 0,31
***
E
CD8 CD66b
5 µm
GzmK
CD8 Not-CD8
31,63 ± 2,84 22,88 ± 0,55
**
F
GZMK+
CTR 1:1 1:10 1:1 TRANS
G
R2: 0.6527
p: <0.0001
%GZMK+ CD8+
%Functional Neutrophils
H
GZMK MFI
CTR 1:1 BM 1:1 TAN
I
R2: 0.4780
p: 0.0004
%GZMK+ CD8+
Tumor Size
J
NEU
CD8
1:1
DAPIE-Cad
E-Cad
ECad rMFI
Neutri CD8 Coco
K
CTR
GzmK
DAPI E-Cad
E-Cad
% A ECad/A DAPI
CTR GZMK
L
LN
HN
DAPI E-Cad
E-Cad
Area um2
LN HN

Figure 4

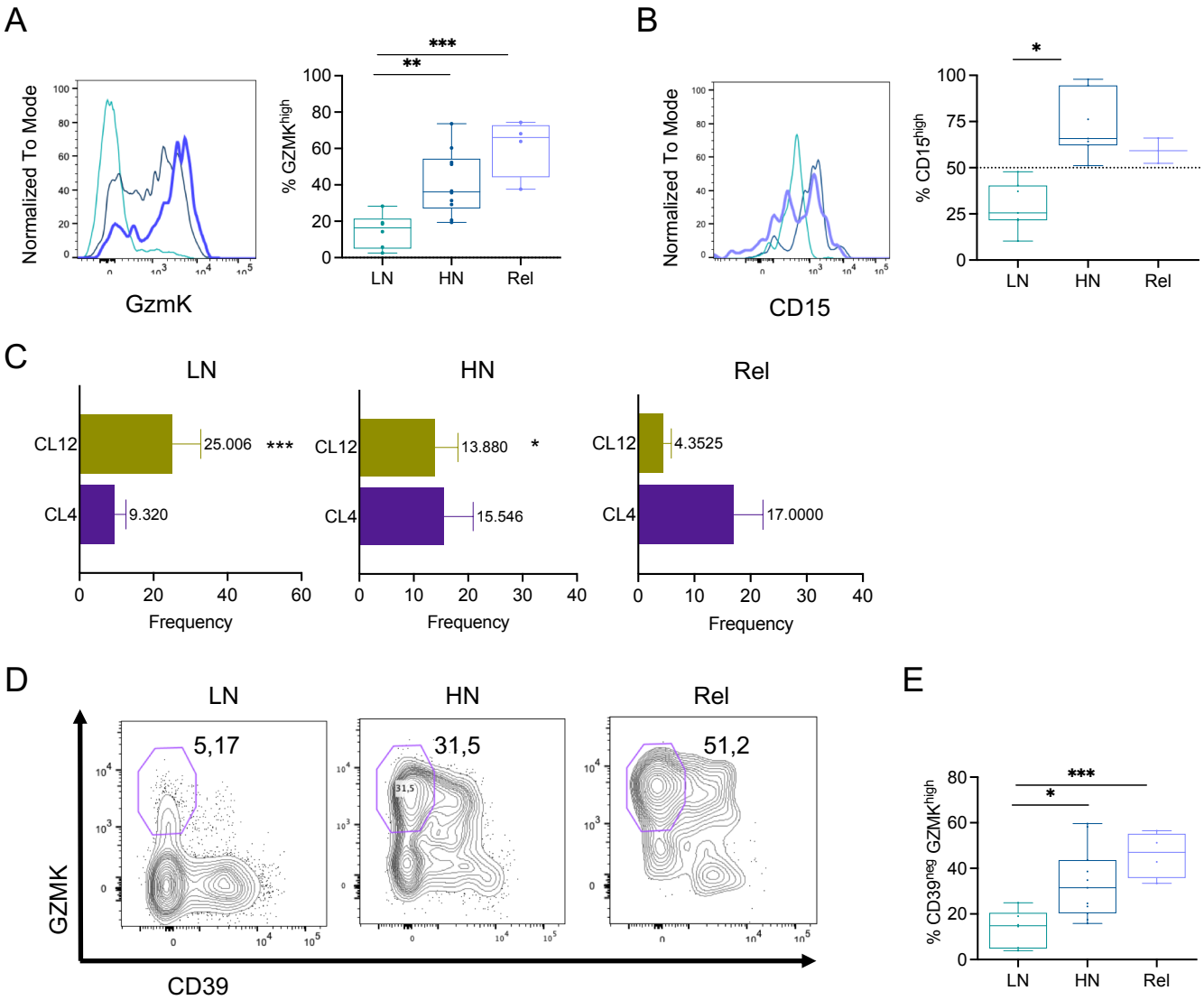
A
Normalized To Mode
GzmK
% GZMK^high
***
**
LN
HN
Rel
B
Normalized To Mode
CD15
% CD15^high
*
LN
HN
Rel
C
LN
HN
Rel
CL12
CL4
25.006
***
9.320
13.880
*
15.546
4.3525
17.0000
Frequency
D
LN
HN
Rel
5,17
31,5
51,2
GZMK
CD39
E
% CD39^neg GZMK^high
***
*
LN
HN
Rel

Figure 5

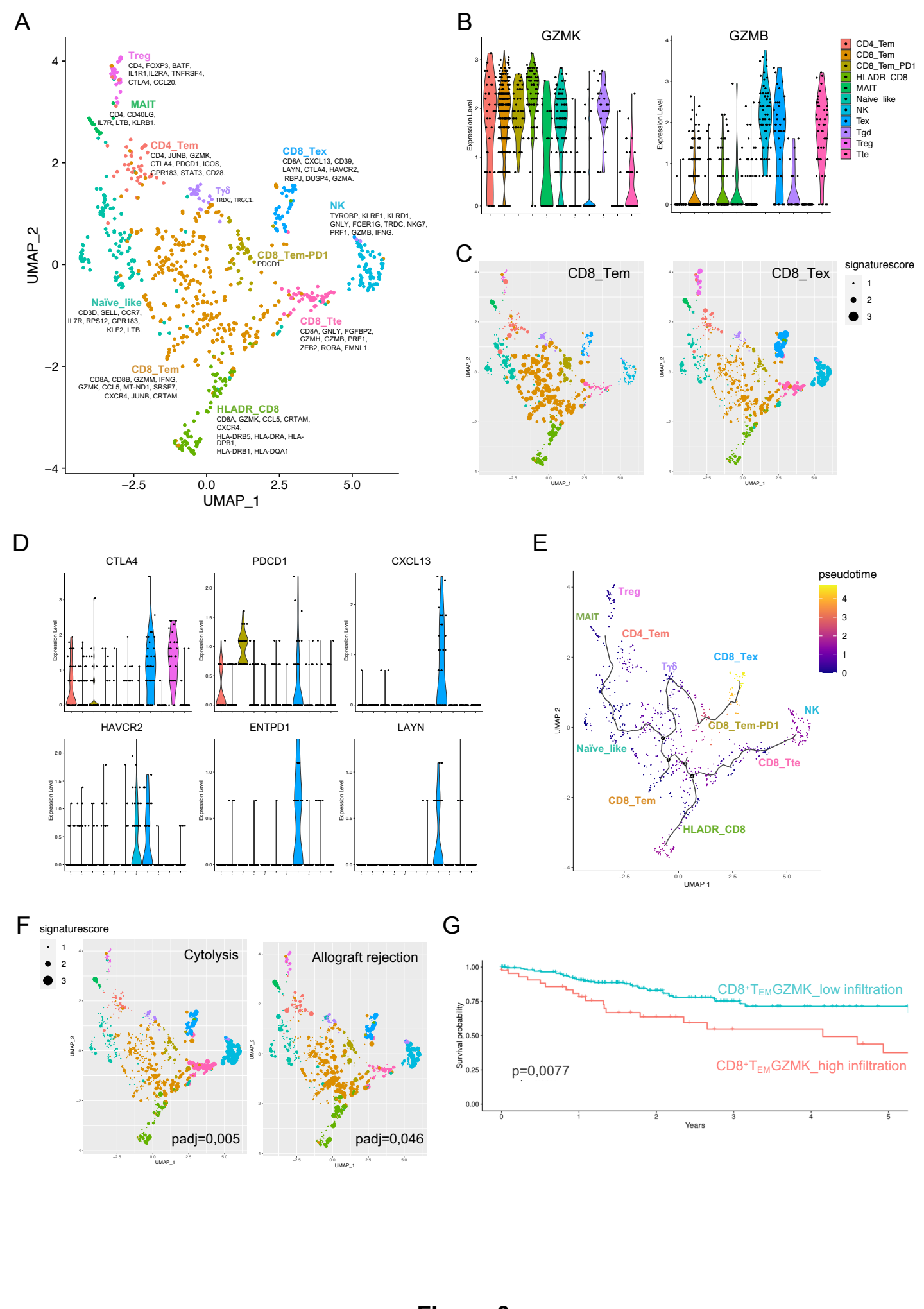
A
Treg
CD4, FOXP3, BATF, IL1R1,IL2RA, TNFRSF4, CTLA4, CCL20.
MAIT
CD4, CD40LG, IL7R, LTB, KLRB1.
CD4_Tem
CD4, JUNB, GZMK, CTLA4, PDCD1, ICOS, GPR183, STAT3, CD28.
Tγδ
TRDC, TRGC1.
CD8_Tex
CD8A, CXCL13, CD39, LAYN, CTLA4, HAVCR2, RBPJ, DUSP4, GZMA.
NK
TYROBP, KLRF1, KLRD1, GNLY, FCER1G, TRDC, NKG7, PRF1, GZMB, IFNG.
CD8_Tem-PD1
PDCD1
Naïve_like
CD3D, SELL, CCR7, IL7R, RPS12, GPR183, KLF2, LTB.
CD8_Tte
CD8A, GNLY, FGFBP2, GZMH, GZMB, PRF1, ZEB2, RORA, FMNL1.
CD8_Tem
CD8A, CD8B, GZMM, IFNG, GZMK, CCL5, MT-ND1, SRSF7, CXCR4, JUNB, CRTAM.
HLADR_CD8
CD8A, GZMK, CCL5, CRTAM, CXCR4.
HLA-DRB5, HLA-DRA, HLA-DPB1,
HLA-DRB1, HLA-DQA1
UMAP_2
UMAP_1
B
GZMK
GZMB
Expression Level
CD4_Tem
CD8_Tem
CD8_Tem_PD1
HLADR_CD8
MAIT
Naive_like
NK
Tex
Tgd
Treg
Tte
C
CD8_Tem
CD8_Tex
signaturescore
1
2
3
UMAP_2
UMAP_1
D
CTLA4
PDCD1
CXCL13
HAVCR2
ENTPD1
LAYN
Expression Level
E
pseudotime
Treg
MAIT
CD4_Tem
Tγδ
CD8_Tex
NK
CD8_Tem-PD1
Naïve_like
CD8_Tte
CD8_Tem
HLADR_CD8
UMAP 2
UMAP 1
F
signaturescore
1
2
3
Cytolysis
padj=0,005
Allograft rejection
padj=0,046
UMAP_2
UMAP_1
G
Survival probability
CD8⁺T_EM GZMK_low infiltration
CD8⁺T_EM GZMK_high infiltration
p=0,0077
Years

Figure 6

Study Cohort		
	Count	Frequency (%)
Total of patients	42	100
Relapse (2 years)	4	9,5
MSI	6	14,3
Age		
<50	2	4,8
50-70	22	52,4
>70	18	42,9
Gender		
F	20	47,6
M	22	52,4
Stage first diagnosis		
I	9	21,4
II	15	35,7
III	18	42,9
BMI		
Normal	19	45,2
Overweight	15	35,7
Obese	7	16,7
NA	1 (NT14)	2,4
Site of primary tumor		
Left	18	42,8
Right	23	54,8
Medium Transverse Colon	1	2,4
Tumor Type		
Adenocarcinoma	39	92,9
Mucinous adenocarcinoma	3	7,1

Table 1. CRC patients' characteristics. Age, Gender, Stage at first diagnosis, Body Mass Index (BMI), Site of primary tumor and Tumor type are shown for the study cohort.

Marker	Fluorophore	Manufacturer	Cat. #
Zombie Aqua		BioLegend	423101
TCRgd	PerCP-Cy5.5	BioLegend	331224
NKG2A	FITC	Miltenyi	130-113-568
CD39	APC-H7	BioLegend	328226
TIGIT	APC	BioLegend	372706
CD25	BV786	BD	741035
CCR7	BV711	BD	566602
OX40	BV650	BD	563658
CD161	BV605	Biolegend	339916
CD27	BV570	BioLegend	302825
CD11b	BV510	Biolegend	301334
PD1	BV480	BD	566112
CD103	BV421	BioLegend	350214
CD8	BUV805	BD	564912
CD28	BUV737	BD	564438
HLADR	BUV661	BD	565073
CD4	BUV615	BD	624297
CD45RA	BUV563	BD	565702
CD3	BUV496	BD	564809
CD69	BUV395	BD	564364
CD45	PE-Cy7	Biolegend	304016304016
CD56	PE-CY5.5	eBioscience	35-0567-42
CD127	PE-CY5	eBioscience	15-1278-42
CX3CR1	PECF594	Biolegend	341624
GZMB	APC-R700	BD	560213
GZMK	PE	Santa Cruz	sc-56125

Table 2. Markers Multiparametric Flow Cytometry panel. Markers with the corresponding Fluorophore, Manufacturer and Catalog ID (Cat. #) are shown.